



HAL
open science

Manipulating Stem Cell Fate with Disordered Bioactive Cues on Surfaces: The Role of Bioactive Ligand Selection

Yujie Zhang, Murielle Remy, Thierry Leste-Lasserre, Marie-Christine Durrieu

► **To cite this version:**

Yujie Zhang, Murielle Remy, Thierry Leste-Lasserre, Marie-Christine Durrieu. Manipulating Stem Cell Fate with Disordered Bioactive Cues on Surfaces: The Role of Bioactive Ligand Selection. *ACS Applied Materials & Interfaces*, 2024, 16 (15), pp.18474-18489. 10.1021/acsami.4c00262 . inserm-04667941

HAL Id: inserm-04667941

<https://inserm.hal.science/inserm-04667941v1>

Submitted on 5 Aug 2024

HAL is a multi-disciplinary open access archive for the deposit and dissemination of scientific research documents, whether they are published or not. The documents may come from teaching and research institutions in France or abroad, or from public or private research centers.

L'archive ouverte pluridisciplinaire **HAL**, est destinée au dépôt et à la diffusion de documents scientifiques de niveau recherche, publiés ou non, émanant des établissements d'enseignement et de recherche français ou étrangers, des laboratoires publics ou privés.



Distributed under a Creative Commons Attribution 4.0 International License

Manipulating Stem Cell Fate with Disordered Bioactive Cues on Surfaces: The Role of Bioactive Ligand Selection

*Yujie ZHANG, Murielle REMY, Thierry LESTE-LASSERRE, Marie-Christine DURRIEU**

ABSTRACT:

The development of 2D or 3D bioactive platforms for rapidly isolating pure populations of cells from adult stem cells holds promise for advancing understanding of cellular mechanisms, drug testing, and tissue engineering. Over the years, methods have emerged to synthesize bioactive micro- and nanostructured 2D materials capable of directing stem cell fate.

We introduce a novel method for randomly micro or nanopatterning any protein/peptide onto both 2D and 3D scaffolds via spray technology. Our goal is to investigate the impact of arranging bioactive micropatterns (ordered vs. disordered) on surfaces to guide human mesenchymal stem cell (hMSCs) differentiation. The spray technology efficiently coats materials with controlled, cost-effective bioactive micropatterns in various sizes and shapes.

BMP-2 mimetic peptides were covalently grafted, individually or in combination with RGD peptides, onto activated polyethylene terephthalate (PET) surfaces through a

spraying process, incorporating nano/micro-scale parameters like size, shape, and composition. The study explores different peptide distributions on surfaces and various peptide combinations. Four surfaces were homogeneously functionalized with these peptides (M1 to M4 with various densities of peptides), and 6 surfaces with disordered micro- and nanopatterns of peptides (S0 to S5 with different sizes of peptide patterns) were synthesized.

Fluorescence microscopy assessed peptide distribution, followed by hMSC culture for 2 weeks, evaluating osteogenic differentiation via immunocytochemistry and RT-qPCR for osteoblast and osteocyte markers.

Cells on uniformly peptide-functionalized surfaces exhibited cuboidal forms, while those on surfaces with disordered patterns tended towards columnar or cuboidal shapes. Surfaces S4 and S5 showed dendrite-like formations resembling osteocyte morphology.

S5 showed significant overexpression of osteoblast (OPN) and osteocyte markers (E11, DMP1, and SOST) compared to control surfaces and other micropatterned surfaces. Notably, despite sharing an equivalent quantity of peptides with a homogeneous functionalized surface, S5 displayed a distinct distribution of peptides, resulting in enhanced osteogenic differentiation of hMSCs.

KEYWORDS: Spray; Micropatterning; Surface modification; Peptides; Cell differentiation

INTRODUCTION

In the past decade, stem cells, with their ability to differentiate into various types of cells, have been proven to be resourceful in regenerative medicine and tissue engineering.^{1, 2} The human mesenchymal stem cells (hMSC), known for their multipotent nature, have been extensively employed in experimental cell therapy and tissue engineering due to their capability to differentiate into diverse lineages, including chondrocytes (cartilage cells), osteoblasts (bone cells), adipocytes (fat cells), and myocytes (muscle cells). The hMSCs possess the ability to generate various stages of bone cell populations, encompassing the MSC, characterized osteoprogenitor cell, preosteoblast, osteoblast, and ultimately, the osteocyte.^{3, 4} Despite the ability to repair damaged parts of organs and tissues, the use of stem cells still entails several limitations, such as low differentiation efficiency and difficulties in guiding differentiation. Unspecialized stem cells, particularly hMSCs, have garnered significant interest in bone tissue engineering owing to their distinct properties of self-renewal, differentiation, high proliferation, pluripotency, ease of acquisition, and lack of ethical concerns. An essential question that still lacks an answer today is how to precisely control the growth and differentiation ability of stem cells, which is crucial in MSC therapy.

The behavior of MSCs, such as cell morphology, differentiation, proliferation, and migration, can be affected by many factors in the extracellular matrix (ECM), including chemistry, stiffness, topography, etc.^{5, 6} The ECM is a very complex environment structured at a micro- and nanometer scale. Nanotechnology approaches have been

recently implemented in stem cell research. It has been discovered that stem cells, in combination with bioactive micro-, nano-patterned materials, show enhanced regenerative performances in varying shape, size, distribution of the patterns and the choice of the biomolecules.⁷⁻¹⁰

The possibility of obtaining 2D or 3D bioactive platforms to rapidly derive pure populations of cells from adult stem cells would lead to significant advancements in understanding cellular mechanisms, as well as in drug testing and tissue engineering.

For several decades, various methodologies have been developed to enable the synthesis of micro-, nanostructured 2D materials. The common element among all these methodologies is the bioconjugation of bioactive elements, which uses different micro-, nano-patterning techniques to spatially confine cells by defining pattern sizes and geometries on the substrate.¹¹

Dip pen nanolithography (DPN) is a scanning probe lithography technique where bioactive molecules are deposited onto the tip of a 'pen' and used to directly write onto high-resolution surfaces, allowing for precise control over patterns at varying scales and densities to influence cell behavior.¹²⁻¹⁴ However, DPN has limitations in creating both micro- and nano-hybrid dimensions simultaneously and is relatively low-throughput due to its slow and serial patterning nature.

Photolithography (PL) is a precise but expensive manufacturing process that uses light to pattern features on thin films or substrates coated with photosensitive material. Despite its high precision, PL has limitations such as the diffraction limit of light,

restricting pattern resolution, and inapplicability to non-flat surfaces. PL has been widely used to study the effects of micropatterned surfaces on cell behavior, enabling the synthesis of materials with micropatterns at a molecular level.¹⁵⁻¹⁷

Electron beam lithography (EBL) utilizes electrons instead of light for resist exposure, achieving high-resolution patterns without requiring masks. The features transferred to the resist in EBL are determined by the exposure pattern design, allowing for highly ordered symmetric patterns, as well as nanoscale patterns with varying degrees of disorder and definable semi-random patterns. While EBL offers high precision, the equipment is costly and time-consuming. Dalby et al. demonstrated an interesting study using EBL to create ordered to disordered nanoscale patterns on polymethylmethacrylate (PMMA), revealing that MSCs cultured on surfaces with disordered patterns exhibited a more typical polygonal osteoblastic morphology and higher osteogenic potential compared to surfaces with ordered patterns.¹⁸

Nanoimprint lithography (NIL) offers high throughput and scalability, enabling precise patterning of diverse geometrical features and materials at ultrahigh resolutions.^{19,20} However, disadvantages include pattern degradation upon repeated use of the mold and the necessity for additional processing to remove residual layers from the substrate. NIL has been used to generate nanogrooves on polyurethane acrylate (PUA) and PMMA for stem cell studies by Yang et al.²¹ and Yim et al.,²² respectively.

All these techniques allow the creation of micro- and nanopatterns of biomolecules on material surfaces by employing a mask, mold, or stamp. We present a novel method

enabling random micro or nanopatterning of any protein/peptide onto polymer surface using spray technology. Our aim is to explore the impact of arranging bioactive micropatterns (ordered vs. disordered) on the surface to regulate stem cell differentiation. The spray technology efficiently coats polymer surfaces with controlled, economically feasible bioactive micropatterns of various sizes and shapes. This spray technique offers, for example, a practical approach to creating hierarchically structured, mechanically durable superhydrophobic surfaces.^{23, 24} The wetting properties, morphology, and mechanical durability of the coatings were systematically studied based on the solvent, suspension composition, and spray-coating distance. Limited publications have explored the use of spray techniques for obtaining micropatterned surfaces with biological applications. For instance, Gagne et al. micropatterned peptides (CGRGDS and CWQPPRARI) onto PTFE samples, creating dots of approximately 10 μ m in diameter. The dot size could be controlled, but the position was random. While sprayed ePTFE with various cell adhesive peptides holds promise for enhancing the endothelialization of Gore-Tex grafts, transitioning this technology from flat surfaces to tubes has not been addressed in existing literature, posing a challenge for its application in vessel lumens.^{25, 26} Our study marks the first application of spray technology in synthesizing disordered bioactive micro/nanopatterned surfaces to evaluate their influence on hMSCs differentiation. While many studies concentrate on disordered topographical cues, our preliminary results, utilizing spray technology to generate disordered bioactive micro/nanopatterned surfaces (PET-spray incorporating BMP-2 cues surrounded by

RGD), emphasized one PET-Spray condition. On this surface, there were 52.1% of BMP-2 spots ranging from 0 to 10 μm , 26.7% from 10 to 20 μm , 6.8% from 20 to 30 μm , 0.7% from 30 to 40 μm , 2.7% from 40 to 50 μm , and 11% of spots exceeding a 50 μm diameter. This surface featuring disordered bioactive cues demonstrated, for the first time in a 2D, an overexpression of osteocyte markers after 2 weeks of culture ; it is generally accepted that the transition from osteoblasts to osteocytes requires a 3D environment.²⁷ Our system is capable of generating a range of random disordered patterns by regulating physical parameters, including air pressure, nozzle-to-substrate distance, liquid flow rate, and spraying duration.

Beyond the distribution of surface-bound ligands, various extracellular matrix (ECM) proteins play pivotal roles in governing the fate of adult stem cells. This new study aimed to replicate the extracellular matrix by primarily focusing on covalently immobilizing RGD and BMP-2 mimetic peptides onto the PET surface.¹⁷⁻²¹ PET, by nature, lacks inherent cell adhesion properties. Hence, the RGD peptide, a well-known adhesion peptide, was used to facilitate cell attachment.²⁸⁻³¹ Conversely, BMP-2 peptides can trigger cell membrane receptors, directing MSCs towards osteoblastic differentiation.^{29, 30, 32} Notably, the FDA approves BMP-2 protein as an osteoinductive growth factor.^{15, 34} However, uncontrolled peptide release can lead to complications like heterotopic bone formation and inflammation. To address this, BMP-2 peptides were covalently grafted individually or in combination with a second peptide (RGD peptides) onto activated PET surfaces through a spraying process, incorporating nano/micro-scale parameters like size, shape, and composition.

This study aims to assess how the distribution of peptide patterns on a polymer surface influences the differentiation of human mesenchymal stem cells (hMSCs). We hypothesize that both the distribution and the specific peptides immobilized play a role. Our research suggests investigating various peptide combinations, such as RGD and BMP-2, and assessing their impact on hMSC differentiation into osteoblasts. Immunocytochemistry and RT-qPCR were employed to analyze early and late osteoblast and osteocyte markers for osteogenic differentiation.

EXPERIMENTAL SECTION

Materials. PET were taken from a commercial crystalline biaxially oriented film obtained from Goodfellow. The thickness of bioriented film is 0.1 mm. Dimethylaminopropyl-3-ethylcarbodiimideethylcarbodiimide hydrochloride (EDC), N-hydroxysuccinimide (NHS), and 2-(N-morpholino)-ethanesulfonic acid (MES) were obtained from Sigma-Aldrich (France). Native and TAMRA-labelled peptides KGRGDSPC(RGD), K(TAMRA)-GRGDSPC (RGD-TAMRA), and KIPKASSVPTELSAISMLYLK(BMP-2), KIPKASSVPTELSAISMLYLK(TAMRA) (BMP-2-TAMRA) peptides were synthesized by GeneCust (Boynes, France). The human Mesenchymal Stem Cells (hMSCs) from bone marrow, human Osteoblasts (OB), Mesenchymal stem cell growth medium 2, SupplementMix MSC growth medium 2, MSC osteogenic differentiation medium, SupplementMix MSC osteogenic diff. medium and osteoblast growth medium, and Supplement Mix osteoblast growth medium were purchased from PromoCell GmbH (Heidelberg, Germany). Dulbecco's modified eagle Medium (D-MEM), Dulbecco's phosphate buffered saline (1X) (PBS),

Trypsin-EDTA and Fetal bovine serum (FBS) were purchased from Thermo Fisher Scientific (France). Tween 20, Triton X-100, Bovine serum albumin (BSA), and Trypan Blue solution were obtained from Sigma (USA). Antibiotic/Antimycotic solution were obtained from GE Healthcare Life Sciences (USA). Alexa Fluoroshield™ 488 Phalloidin, Secondary antibodies (Goat anti-Mouse IgG (H+L) Highly Cross-Adsorbed Secondary Antibody Alexa Fluoroshield™ 647 and Goat anti-Rabbit IgG (H+L) Highly Cross-Adsorbed Secondary Antibody Alexa Fluoroshield™ 647), and DAPI were purchased from Thermo Fisher Scientific (USA). Primary antibody against RUNX2 Rabbit mAb was acquired from Cell Signaling (USA). Mouse anti-osteopontin (OPN) was bought from Santa Cruz Biotechnology (USA). Mouse monoclonal anti-podoplanin (E11) antibody and Rabbit polyclonal anti-Sclerostin (SOST) were purchased from Abcam (EL ROZENBURG, Germany). DMP1 monoclonal antibody (DMP1) was purchased from Abnova (Taiwan, China).

Preparation of PET. PET was modified according to our previous protocol.³² Briefly, the clean PET was immersed in EDC/NHS/MES activation solution (EDC (0.2M), NHS (0.1M) and MES (0.1M) in ultrapure water. The carboxyl groups on the PET surface were activated, denoted as "PET-Activated" (Fig. 1).

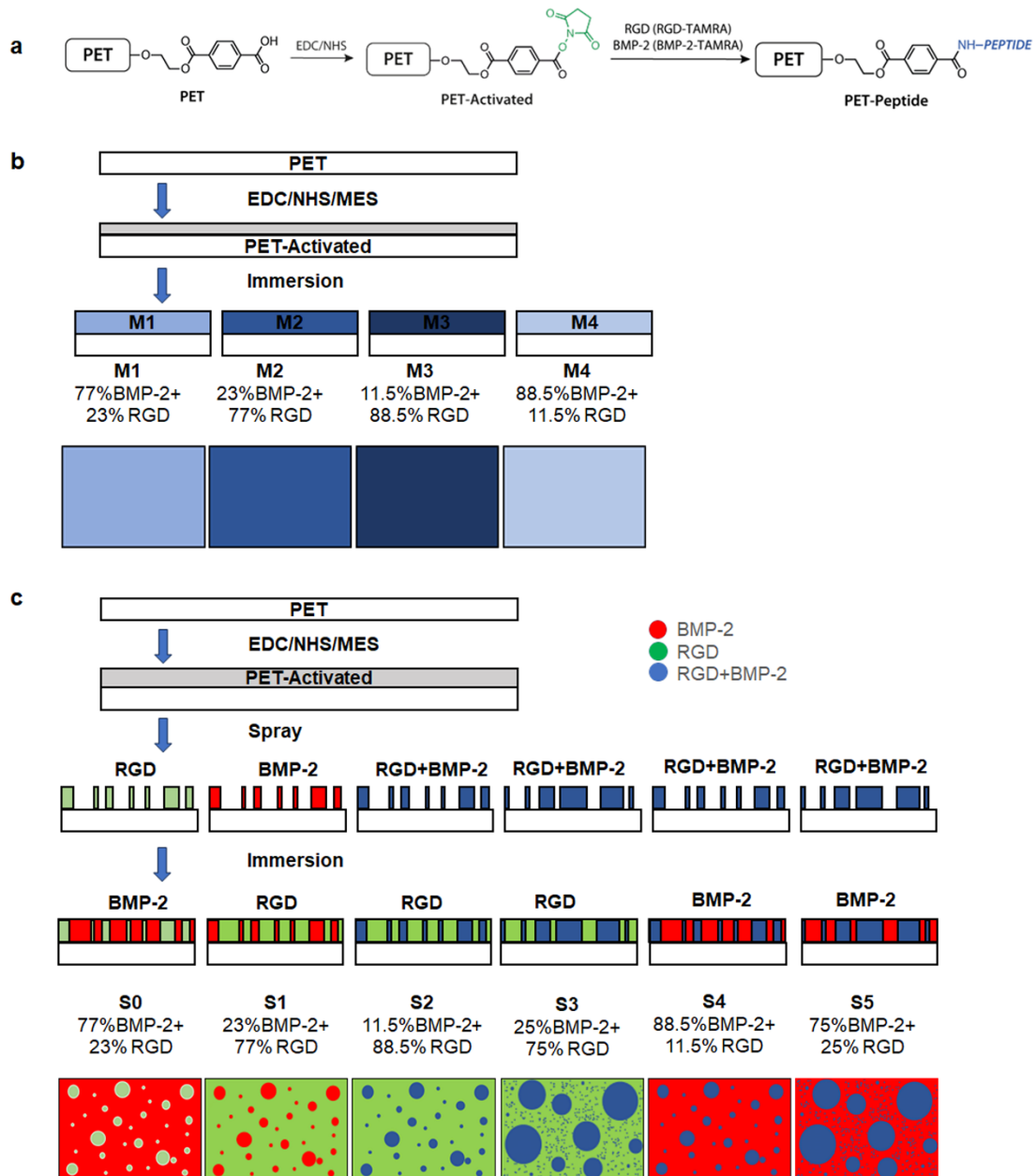


Fig. 1 Peptide immobilization onto PET surfaces. a) Scheme of PET functionalization with peptide; b) Scheme of preparation of the homogenous peptide surfaces. Different sample colours represent different BMP-2+RGD contents: light blue (M1) has 77% BMP-2+23%RGD, blue (M2) has 23% BMP-2+77%RGD, dark blue (M3) has 11.5% BMP-2+88.5% RGD, sky blue (M4) has 88.5% BMP-2+11.5% RGD; c) Scheme of preparation of the disordered peptide micropattern surfaces.

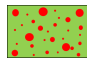

Spray technology. We constructed a homemade spray prototype using an automatic spray gun (PILOT WA 450, WALTHER Spritz- und Lackiersysteme GmbH, Germany) mounted on a rail.³² The spray gun was connected to an air cap (0.3-1.8mm,

V1136030050*) and regulated by a pressure regulator (BD-26-8-6) ranging from 0.5 bar to 4 bar for controlling air pressure. A syringe pump (R99-EB, Razel Scientific Instruments) was interposed between the spray gun and a 10cc/mL or 20cc/mL Terumo syringe without a needle (Terumo Europe N.V.). The syringe pump allowed control of the liquid flow speed ranging from 50 μ l/min to 1650 μ l/min. PET was positioned on an adjustable table (PROLABO), enabling a maximum displacement of 30 cm to set the distance between the nozzle and the material, although a 20 cm distance was maintained for all experiments. The syringe's liquid, controlled by the pump, was conveyed into the spray chamber at a specific flow rate and then atomized into micro-nano droplets by passing nitrogen at a specific pressure. These droplets were sprayed onto the PET surface through a nozzle. Consequently, a series of semi-random droplets with disordered nano/micro patterns were obtained on the PET.

Surface functionalization. As previously described,³² all peptides were first dissolved in DMSO, and then diluted to the desired concentration in ultrapure water. To synthesize homogeneous bioactive surfaces, the activated surface "PET-Activated" was immersed for 16 hours at room temperature in a solution of RGD-TAMRA or BMP-2-TAMRA, or a solution containing both RGD and BMP-2 peptides (Four different ratios of each peptide were used). After covalent immobilization, the surfaces were sonicated 6 times with ultrapure water for 15 min to remove the physically attached peptides. The resulting materials were called "PET-RGD", "PET-BMP", "PET-M1" or simply "M1" (comprising 77% BMP-2+23% RGD on the surface), "PET-M2" or simply "M2" (comprising 23% BMP-2+77% RGD), "PET-M3" or

simply “M3” (comprising 11.5% BMP-2+88.5% RGD), “PET-M4” or simply “M4” (comprising 88.5% BMP-2+11.5% RGD) (Table 1).

Table 1. Peptide contents in different homogeneous and disordered combination peptide patterns

	Air pressure, flow speed, time	Micropattern content	Outside content of micropattern	RGD	BMP-2	Surface illustrations
S0	1bar,200μl/min,3s	23% RGD	77% BMP-2	23%	77%	
S1	1bar,200μl/min,3s	23% BMP-2	77% RGD	77%	23%	
S2	1bar,200μl/min,3s	23% Mix of BMP-2 and RGD	77% RGD	88.5%	11.5%	
S3	0.5bar, 450μl/min,3s	50% Mix of BMP-2 and RGD	50% RGD	75%	25%	
S4	1bar,200μl/min,3s	23% Mix of BMP-2 and RGD	77% BMP-2	11.5%	88.5%	
S5	0.5bar, 450μl/min,3s	50% Mix of BMP-2 and RGD	50% BMP-2	25%	75%	
M1	23% RGD+ 77% BMP-2			23%	77%	
M2	77% RGD+ 23% BMP-2			77%	23%	
M3	88.5% RGD+ 11.5% BMP-2			88.5%	11.5%	
M4	11.5% RGD+ 88.5% BMP-2			11.5%	88.5%	

BMP-2	
RGD	
Mix	

Peptides for spraying were prepared at a concentration of 10 μ M in a 7.5% glycerol solution. When a mixture of peptides is used, the peptide solution contains 50% of RGD and 50% of BMP-2. These conditions were selected not only to ensure viscosity compatible with the injection system but also to control rapid evaporation, enabling the covalent immobilization of peptides on the PET surface. The micropattern distribution was controlled by adjusting the distance between the spray nozzle and the material, liquid flow speed, spray duration, and air pressure. Following the spraying process, PET-Spray surfaces were maintained at 4°C in darkness for 4 days to prevent excessive evaporation and enhance peptide density on the PET surface. Subsequently, the surfaces underwent sonication six times with ultrapure water for 15 minutes each to remove physically attached peptides.

Six different PET surfaces were prepared by varying not only the size of the micropatterns but also the distribution of the peptides (Table 1):

PET-S0: Sprayed with RGD peptides at 1 bar, 50 μ l/min, 3 s, followed by grafting through immersion with BMP-2 peptides (comprising 77% BMP-2+23% RGD).

PET-S1: Sprayed with BMP-2 peptides at 1 bar, 50 μ l/min, 3 s, followed by grafting through immersion with RGD peptides (comprising 77% RGD+23% BMP-2).

PET-S2: Sprayed with a MIX of RGD and BMP-2 peptides at 1 bar, 50 µl/min, 3 s, followed by grafting through immersion with RGD peptides-(comprising 11.5% BMP-2+88.5 % RGD).

PET-S3: Sprayed with a MIX of RGD and BMP-2 peptides at 0.5 bar, 300 µl/min, 3 s, followed by grafting through immersion with RGD peptides (comprising 25 % BMP-2+ 75% RGD).

PET-S4: Sprayed with a MIX of RGD and BMP-2 peptides at 1 bar, 50 µl/min, 3 s, followed by grafting through immersion with 77% BMP-2 peptides (comprising 88.5 % BMP-2+ 11.5% RGD).

PET-S5: Sprayed with a MIX of RGD and BMP-2 peptides at 0.5 bar, 300 µl/min, 3 s, followed by grafting through immersion with BMP-2 peptides (comprising 75 % BMP-2+ 25% RGD).

Evaluation of Peptide Density by Fluorescence Microscopy. The assessment of peptide density immobilized on the PET surface was conducted through fluorescence microscopy (using a Leica DM5500B microscope, Germany). For this purpose, fluorescent peptides (linked to fluorescent dyes through lysine (K)) were immobilized onto PET following our established protocol as described in our previous publications.^{21,22-24,27} To quantify the covalently grafted peptides, PET surfaces were functionalized with RGD-TAMRA, BMP-2-TAMRA, a combination of BMP-2-TAMRA and RGD, and a mix of BMP-2 and RGD-TAMRA. Post-washing, the fluorescent peptides grafted on the PET surface were observed using fluorescence

microscopy at a 10x objective with configured parameters including Bin3, Gain2, and an exposure time of 1000 ms, consistently applied across all images. Each sample underwent triplicate preparation, with analysis conducted on 10 distinct areas per sample.

The Image J software was employed to quantify the fluorescence intensity of peptide-TAMRA grafted onto the PET surface. A calibration curve in pmol/mm² was generated to ascertain the density of each fluorescent peptide immobilized on the surface. This involved depositing droplets of RGD-TAMRA and BMP-2-TAMRA peptides with known concentrations (ranging from 10 nM to 10 μM) onto pristine PET surfaces (the volume of each drop was 0.3 μl). Subsequently, these peptide droplets were imaged using the same objective and exposure time settings, establishing individual standard curves for each peptide.

The quantification of fluorescence intensity on various peptide-modified surfaces was performed using Image J software, with the peptide density calculated based on the established standard curve in pmol/mm².

Cell Culture. All materials were sterilized using 70% ethanol overnight. The human mesenchymal stem cells (hMSCs) were thawed and cultured in mesenchymal stem cell growth medium 2 under 5% (vol/vol) CO₂ at 37 °C in a humidified environment. Subsequently, cells were subcultured by employing 0.25% Trypsin/EDTA 1x for detachment.

For cell differentiation experiments, hMSCs were seeded onto sterilized materials in DMEM medium without serum at a density of 2000 cells/cm² during 6 hours. At the end of this incubation period 10% (vol/vol) FBS was added. After 24 hours, the medium was replaced with DMEM containing 10% (vol/vol) FBS or hMSC osteogenic differentiation medium supplemented with 1% antibiotic solution for the cell experiments.

The nomenclature used to identify the culture medium is: "D" for osteogenic differentiation medium and "N" for 10% FBS+ DMEM medium without any differentiation medium. Cells were then cultured for 2 weeks, and all the media were replaced twice per week.

The human osteoblasts (OB) were thawed and cultured in osteoblast growth medium. Then OB were seeded on sterilized glass slides at a density of 20,000 cells/cm² in osteoblast growth medium. Finally, the cells were fixed with 4% paraformaldehyde (PFA) at 24 h and 2 weeks, and kept in PBS solution at 4°C for immunofluorescence assays.

The cells were divided into three groups based on the level of disorder. The first group acted as the control, consisting of hMSCs cultured on glass in a 10% FBS/DMEM medium (referred to as "MSC-N"), hMSCs cultured on glass in osteoblast differentiation medium ("MSC-D"), and osteoblasts cultured on glass in osteoblast growth fluid ("OB"). The second group comprised homogeneous surfaces presenting varying ratios of RGD and BMP-2 mimetic peptides ("M1", "M2", "M3", "M4", as

shown in Table 1), where hMSCs were cultured in osteogenic differentiation medium. The third group involved disordered bioactive surfaces created through spray deposition ("S0", "S1", "S2", "S3", "S4", and "S5", featuring diverse combined peptide compositions and distributions (Table 1)), upon which hMSCs were cultured in osteogenic differentiation medium.

Immunocytochemistry analysis. All samples underwent permeabilization with 0.5% Triton/PBS for 15 minutes at 4 °C followed by saturation with 1% BSA/PBS for 30 minutes at 37 °C. Subsequently, cells were incubated in a humidified chamber at 37 °C for 1 hour with various primary antibodies diluted in 1% BSA/PBS: OPN monoclonal antibody (Mouse) at 1 µg/mL, E11 monoclonal antibody (Mouse) at a concentration of 2 µg/mL, SOST monoclonal antibody (Rabbit) at a concentration of 5 µg/mL, and DMP1 monoclonal antibody (Mouse) at a concentration of 10 µg/mL. After washing with 0.05% Tween 20 / PBS, cells were incubated with the secondary antibody: Goat anti-Mouse IgG (H+L) Highly Cross-Adsorbed Secondary Antibody Alexa Fluoroshield™ 647 and Goat anti-Rabbit IgG (H+L) Highly Cross-Adsorbed Secondary Antibody Alexa Fluoroshield™ 647, both at a concentration of 1/400 in 1% BSA/PBS for 1 hour at 37 °C. Subsequent to this, cells were exposed to Alexa Fluoroshield™ 488 Phalloidin at a dilution of 1/40 for 1 hour at 37 °C to visualize cell morphology and cytoskeleton organization. Finally, nuclei were stained with DAPI at a dilution of 1/1000 for 1 hour in the dark at 4°C. The fluorescently stained samples were observed using an epifluorescence microscope (Leica DM5500B) and captured with Metamorph software (10x and 40x Objective). Image J software, available at

www.nih.gov, was used for file conversion to 16-bit format. These fluorescence images were then utilized to measure the red fluorescence intensity emitted by the labels, and background signal was subtracted, calculated from hMSC cultures on PET or glass surfaces incubated solely with the secondary antibody Alexa Fluor 647. Fluorescence intensity measurements were performed on at least 60-80 cells for each surface type.

Additionally, after 24 hours and 2 weeks of culture, cytoskeletons were labeled with Phalloidin to highlight F-actins, while nuclei were stained with DAPI.

The expression of OPN was measured in the nucleus, while the expression of E11, DMP1, and SOST was measured in the whole cell. After quantifying the expression of the differentiation markers by measuring the fluorescence intensity in the cells, we calculated their intensity frequency distribution to display the observations within a given interval of fluorescence intensities for the different samples.

Cell shape. After a 2-week culture period, cell cytoskeletons and nuclei were fluorescently stained, with F-actins highlighted using phalloidin and nuclei marked with DAPI. Parameters such as aspect ratios (ARs), circularities, and anisotropy were quantified by delineating cells in fluorescence images using ImageJ. AR represents the ratio between the major and minor axes of the particle's fitted ellipse, calculated from the two eigenvalues of the cell profile in ImageJ. Circularity quantifies the shape, with a value of 1.0 indicating a perfect circle and decreasing values indicating more elongated shapes.

The alignment of F-actin within cells (anisotropy) was measured using the ImageJ plugin "FibrilTool," following the protocol by Boudaoud et al.^{16, 35} Raw images captured with a fluorescence microscope at a 40x objective were analyzed in ImageJ. A region of interest (ROI) was selected to encompass a single cell, and the FibrilTool plugin was used to gauge the degree of F-actin orientation using an anisotropy parameter ranging from 0 to 1. An anisotropy value of 0 represents disordered F-actin (completely isotropic fibers), while a value of 1 indicates perfectly ordered F-actin fibers (parallel arrangement). These measurements were conducted on 60–80 individual cells per sample.

RT Quantitative real-Time PCR (qPCR). Following a 2-week cell culture period, cells from 24 materials measuring 1 cm² per condition were harvested for these qPCR experiments. The RT-qPCR analyses were performed on the two conditions identified by immunocytochemistry as the most effective in inducing hMSC differentiation towards a bone lineage (M1 and S5). The M1 condition was normalized to 1. RNA samples were extracted and processed with the RNeasy micro kit (Qiagen).³⁶ cDNA was synthesized from 2 µg of total RNA using Maxima Reverse Transcriptase (Fisher Scientific) and primed with oligo-dT primers (Fisher Scientific) and random primers (Fisher Scientific). QPCR was performed using a LightCycler® 480 Real-Time PCR System (Roche, Meylan, France). QPCR reactions were done in duplicate for each sample, using transcript-specific primers, cDNA (4 ng) and LightCycler 480 SYBR Green I Master (Roche) in a final volume of 10 µl. Primers sequences are reported in table 2. For the determination of the reference gene, the RefFinder method was used.³⁷

Relative expression analysis was normalized against two reference genes and the Glyceraldehyde-3-phosphate dehydrogenase (Gapdh) and glucuronidase beta (Gusb) genes were used. The relative level of expression was calculated using the comparative 2- $\Delta\Delta$ CT method.

Table 2. qPCR primer sequences

Gene	GenBank ID	Forward sequence (5'-3')	Reverse sequence (5'-3')
Gapdh	NM_002046	CACCCATGGCAAATTCC	TGGGATTCCATTGATGACAAG
Gusb	NM_000181	CCATCTGGGTCTGGATCAAAA	TGAAATCGGCAAAATTCCAAAT
Runx2	NM_001015051	TAAGGATTCCCTCAATTCCGA	ATGCTTCGTGTTTCCATGT
Pdpm	NM_006474	GCTCGGCCTCAGATTCC	AACTCATCCAGCTCTTCTCA
Spp1	NM_001040058	AACATGAAATGCTTCTTTCTCAGT	ACACATTAGTTATTTCCAGACTCA

Statistical Analysis. Data are means \pm SD of at least three independent trials. Significant differences between treatment means were assessed by one-way ANOVA in Origin (Origin Lab, Northampton, MA, USA). For RT-QPCR analyses, a one-tailed student t-test was used to compare the 2 conditions. Significant differences were determined for p values of at least ≤ 0.05 . * $p \leq 0.05$, ** $p \leq 0.01$, and *** $p \leq 0.001$.

RESULTS

Spray. As previously demonstrated, the peptide droplets sprayed using the spray technique come into contact with the activated PET surface, initiating covalent reactions between the peptides and the surface.³² Our earlier study primarily focused on PET-Spray conditions, which involved spraying with a single mimetic peptide of BMP-2 protein.³² It reported that the S1 condition (sprayed at 1 bar air pressure,

200 μ l/min solution flow rate, and 3s spray time) exhibited the highest osteoblast induction effect. The S1 condition comprised 23% disordered BMP-2 peptide micropatterns and 77% RGD surface coverage.

However, in this latest research initiative, we explored diverse peptide motifs (single peptide (RGD or BMP-2 peptide) or a cocktail of peptides (RGD+BMP-2)). We successfully generated various patterns of different sizes and surface distributions, incorporating different peptide cocktails. To compare the osteoblast induction effects of different peptides under the same micropattern distribution, we designed S0, S1, S2, and S4 as comparison groups. S0 has sprayed micropatterns with RGD peptide only, S1 has sprayed micropatterns with BMP-2 peptide only, S2 has sprayed micropatterns with a cocktail of peptides composed of RGD+BMP-2 peptides, and S4 has sprayed micropatterns with the same cocktail of peptides composed of RGD+BMP-2 peptides. All these surfaces (S0, S1, S2, and S4) present 49.8% of very small micropatterns with a diameter less than 10 μ m, 30.2% with diameters between 10 μ m to 20 μ m, and 7.4% with diameters between 20 μ m and 30 μ m. To explore the impact of a different micropattern distribution on the induction of cells' osteogenic differentiation but with the same RGD and BMP-2 content, we designed another micropattern distribution (S3 and S5) by adjusting air pressure, solution flow rate, and spraying time. For example, S0 has 23% RGD and 77% BMP-2 surface coverage. Therefore, we designed S5 conditions (with the same 23% RGD and 77% BMP-2 surface coverage as S0), which were sprayed at 0.5 bar air pressure, 450 μ l/min solution flow rate, and 3s spray time. The majority of the pattern sizes distributed across 0-10 μ m, 10-20 μ m, and 20-30 μ m droplets comprise 80.3%, 13.8%, and 2.3% of the total droplet count, respectively.

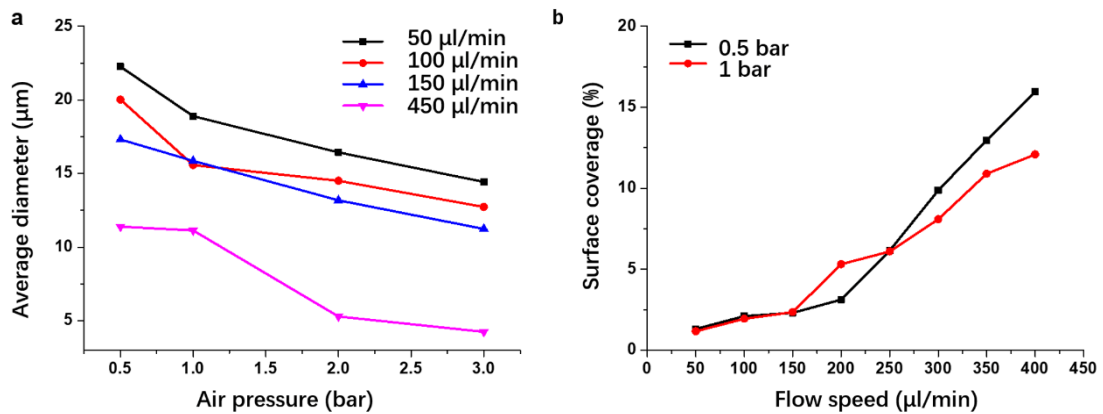


Fig. 2 a) Mean diameter of spots on the surface as a function of atomization pressure at the same spray time: 1s; b) Effect of variation in liquid flow speed on surface coverage and spots mean diameter at the same spray time: 1s.

Our system offers air pressure settings ranging from 0.5 bar to 4 bar. As depicted in Fig. 2a, we examined the patterns generated at different air pressures—0.5 bar, 1 bar, 2 bar, and 3 bar. While maintaining a consistent liquid flow rate and nozzle-to-material spacing, our observations revealed a trend: the average diameter of the resulting pattern decreased as the air pressure increased at the same liquid flow rate. Furthermore, at identical air pressures, a reduced liquid flow rate resulted in larger droplet diameters. Essentially, we found an inverse relationship between air pressure and pattern size, as well as between liquid flow rate and average pattern size.

Following this, we regulated the sprayed liquid volume by modifying the liquid flow rate while keeping parameters like air pressure and nozzle-to-material distance constant. Illustrated in Fig. 2b are the droplet coverages ranging from 50μl/min to 450μl/min. With an increase in the liquid flow rate, there was a corresponding rise in the sprayed liquid volume. We noted a direct relationship between the patterned surface

coverage and the escalated liquid flow rate. Intriguingly, lower air pressure facilitated the generation of larger pattern sizes and increased surface coverage.

Moreover, extending the spraying duration results in an increase in the volume of the sprayed liquid, subsequently allowing for a greater surface coverage. For our cell culture experiments, we selected two parameter configurations for the spray samples: 1 bar, 200 $\mu\text{l}/\text{min}$, 3 s (samples S0, S1, S2, S4) and 0.5 bar, 450 $\mu\text{l}/\text{min}$, 3 s (samples S3, S5).

As shown in Fig. 3a, all the patterns sprayed onto PET at 1 bar, 200 $\mu\text{l}/\text{min}$, 3 s covered approximately 23% of the surface (Table 3). The majority of the pattern sizes fell within the 0-30 μm range, distributed across three size categories: 0-10 μm , 10-20 μm , and 20-30 μm droplets. Droplets larger than 30 μm accounted for 12.6% of the total count, contributing to a surface coverage of 15%.

Table 3. Parameters used for spray technique and the resulting distribution of spot counts (% for each diameter range)

	Air pressure (bar)	Speed ($\mu\text{l}/\text{min}$)	Time (s)	0-10 μm (%)	10-20 μm (%)	20-30 μm (%)	30-40 μm (%)	40-50 μm (%)	50+ μm (%)	Average diameter (%)	Surface coverage (%)
S3/S5	0.5	450	3	80.3 ± 5.7	13.7 ± 2.9	2.3 ± 0.1	1.1 ± 0.9	0.3 ± 0.4	2.4 ± 1.5	13.7 ± 1.8	50.9 ± 0.6
S0/S1/S2/S4	1	200	3	49.8 ± 3.2	30.2 ± 4.9	7.4 ± 0.8	1.8 ± 1.6	4.3 ± 2.3	6.5 ± 6.4	17.9 ± 3.86	23.3 ± 2.8

Fig. 3b illustrates the pattern sprayed on PET at 0.5 bar, 450 $\mu\text{l}/\text{min}$, 3 s. The overall surface coverage of all droplets is 50.9% (Table 3), with the area of larger droplets exceeding 30 μm patterned at a surface coverage of 49%. However, the proportion of larger droplets with a size greater than 30 μm is only 3.8% of the total droplet count. This suggests that the surface sprayed at 0.5 bar, 450 $\mu\text{l}/\text{min}$, 3 s exhibits few but relatively large droplets. Conversely, we observed that 80.3% of the droplet number were concentrated in the 0–10 μm size interval, indicating a large number of small droplets. Condition “1 bar, 200 $\mu\text{l}/\text{min}$, 3 s” shows less variation in this size distribution, where 49.8% of the micropatterns of the total droplet count have a diameter ranging from 0 to 10 μm ; and 30.2% of the micropatterns of the total droplet count have a diameter ranging from 10 to 20 μm (Fig.3).

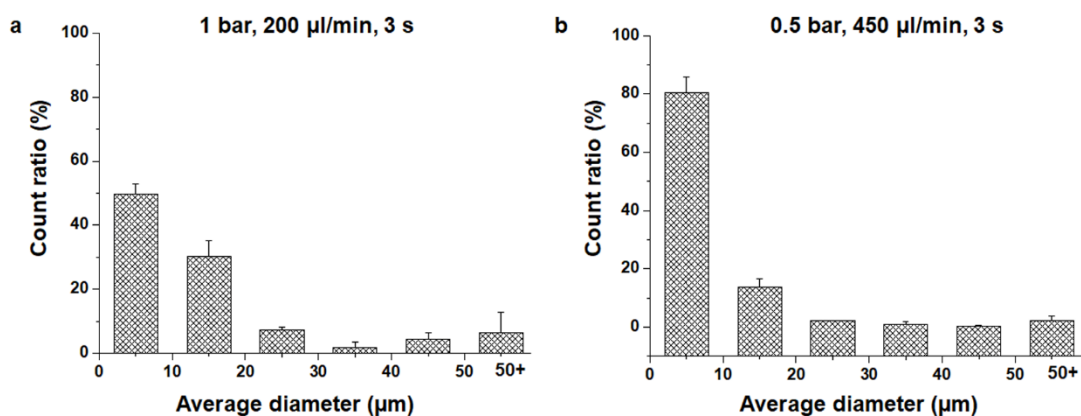


Fig. 3 The count distribution of micropatterns obtained from a) 1 bar, 200 $\mu\text{l}/\text{min}$, 3 s for S0, S1, S2 and S4; b) 0.5 bar, 450 $\mu\text{l}/\text{min}$, 3 s for S3 and S5. S0 and S5 have similar RGD/BMP-2 content.

Fluorescence Microscopy. To evaluate the peptide density within various micropatterns, one of the two peptides was conjugated with TAMRA probes, while the other remained untagged. For instance, in sample S0, we prepared two material subsets: S0-1 (micropatterns obtained after spray application with RGD-TAMRA peptide grafting, while free PET surface regions were grafted with BMP-2 peptides without tag) and S0-2 (micropatterns obtained after spray application with RGD peptide grafting (without tag), while free PET surface regions were grafted with BMP-2-TAMRA). Subsequently, these surfaces were captured using fluorescence microscopy and subjected to analysis using ImageJ. Then, we assessed the density of both RGD and BMP-2 mimetic peptides on the PET surface in sample S0. Sample S0 displayed a BMP-2 peptide density of $0.7 \text{ pmol/mm}^2 \pm 0.2 \text{ pmol/mm}^2$, considering the BMP-2-TAMRA density in sample S0-2. Correspondingly, the RGD peptide density within sample S0 was determined to be $0.1 \text{ pmol/mm}^2 \pm 0.1 \text{ pmol/mm}^2$, taking into account the RGD-TAMRA density from sample S0-1. This same procedure was applied to evaluate the densities of RGD and BMP-2 mimetic peptides grafted onto surfaces S1, S2, S3, S4, and S5. Our findings emphasized the peptide densities on each surface, with (Density BMP-2 peptide + Density RGD peptide) recorded as ($0.5 \text{ pmol/mm}^2 + 0.2 \text{ pmol/mm}^2$), ($0.6 \text{ pmol/mm}^2 + 0.1 \text{ pmol/mm}^2$), ($0.5 \text{ pmol/mm}^2 + 0.2 \text{ pmol/mm}^2$), ($0.1 \text{ pmol/mm}^2 + 0.7 \text{ pmol/mm}^2$), and ($0.2 \text{ pmol/mm}^2 + 0.6 \text{ pmol/mm}^2$) for S1, S2, S3, S4, and S5, respectively (Fig. 4).

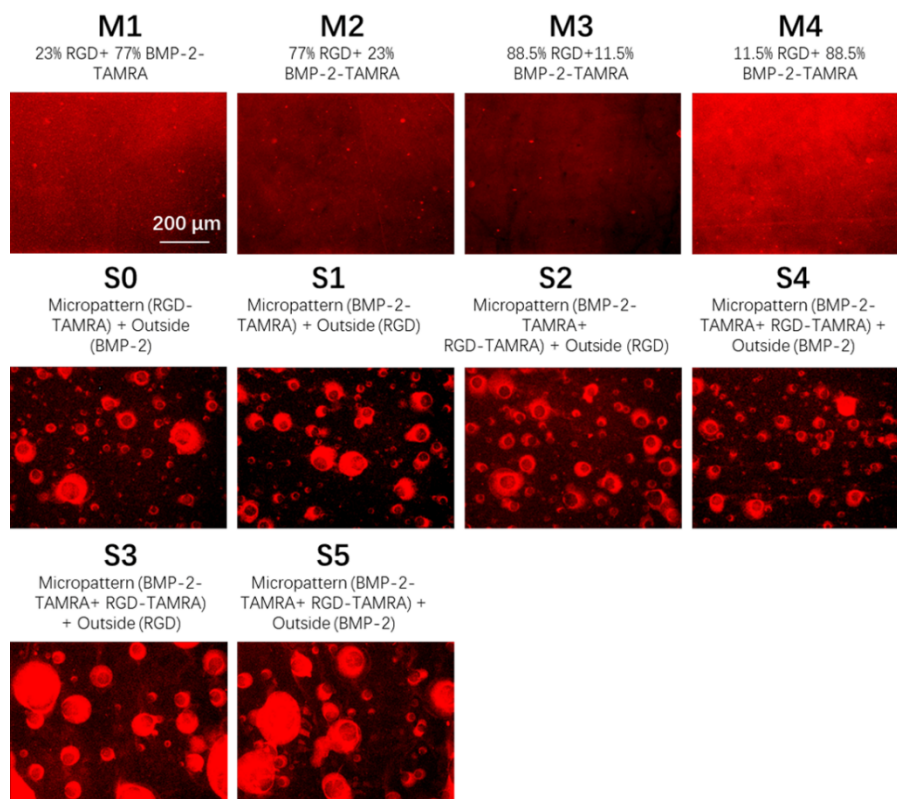


Fig. 4 Fluorescence images obtained from M1, M2, M3, M4, S1, S2, S3, S4, S5. Each line has similar peptide surface distribution, and each column has similar RGD/BMP-2 contents.

For samples uniformly functionalized with peptides, we applied the same methodology. Taking sample M1 as an example, we produced M1-1 (PET surface functionalized with a mixture of 23% RGD and 77% BMP-2-TAMRA) and M1-2 (PET surface functionalized with a mixture of 23% RGD-TAMRA and 77% BMP-2). Consequently, we deduced that M1 contains a RGD peptide density of 0.1 pmol/mm^2 by evaluating the RGD-TAMRA density in M1-2, and a BMP peptide density of 0.6 pmol/mm^2 by assessing the BMP-TAMRA density in M1-1. Similarly, the density of RGD peptides was determined as $0.5 \text{ pmol/mm}^2 \pm 0.1 \text{ pmol/mm}^2$, $0.5 \text{ pmol/mm}^2 \pm 0.2 \text{ pmol/mm}^2$, $0.1 \text{ pmol/mm}^2 \pm 0.1 \text{ pmol/mm}^2$ for materials M2, M3, and M4. The density

of BMP-2 grafted was calculated as $0.2 \text{ pmol/mm}^2 \pm 0.1 \text{ pmol/mm}^2$, $0.1 \text{ pmol/mm}^2 \pm 0.1 \text{ pmol/mm}^2$, $0.7 \text{ pmol/mm}^2 \pm 0.2 \text{ pmol/mm}^2$ for materials M2, M3, and M4.

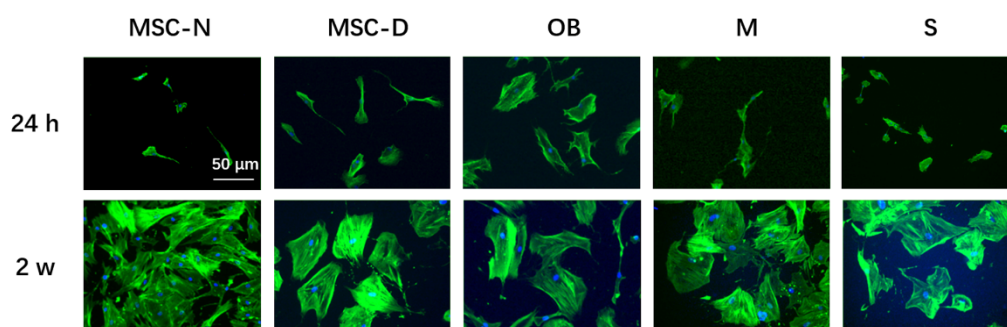


Fig. 5 Fluorescence images of hMSCs cultured for 24 h and 2 weeks on the control group (MSC-N, MSC-D and OB) and on one PET-M1 and one PET-S1. Cells were stained with conjugated phalloidin to detect F-actin (in green) and DAPI (nucleus). Objective 10x, scale bar: 50 μm.

Immunocytochemical analysis. We conducted an analysis to assess how diverse disordered bioactive micro- and nanopatterns, varying in pattern sizes, surface distributions, and peptide combinations, affected the differentiation of human mesenchymal stem cells (hMSCs). This evaluation involved a 2-week culture of hMSCs in osteoblastic differentiation medium, tracking their commitment to an osteoblastic lineage by examining specific markers. We focused on four markers: OPN, indicative of late osteoblasts; E11 and DMP1, serving as early osteocyte markers; and SOST, a marker for late osteocytes. To visualize cell nuclei on the material surface, we used DAPI, while F-actin staining was employed to study cellular morphology and the cytoskeleton by phalloidin.

When comparing the images of hMSCs cultured for 24 hours and 2 weeks (Fig. 5), it's evident that cell proliferation occurred in all conditions except for the "OB"

condition (Fig. 5). As an illustration, we provide images obtained with surfaces M1 and S1 (data not shown for other conditions).

Following a 2-week culture period, the cell morphology in the control group "MSC-N" retained its elongated and flattened shape, which is a characteristic hallmark of hMSCs (Fig 5, Fig. 6a and Fig. 6b). The cells observed on the "MSC-D" control materials exhibited a notable morphological transformation between the 24-hour and 2-week intervals (Fig. 6a and 6b). After 2 weeks, the hMSCs adopted a cuboidal shape, indicative of osteoblast cells (Fig. 6.6a and 6.6b). Consistency in morphology was observed among the seeded osteoblasts on the control material "OB" at both 24 hours and 2 weeks, where they consistently maintained their cuboidal shape as anticipated (Fig. 6a and 6b).

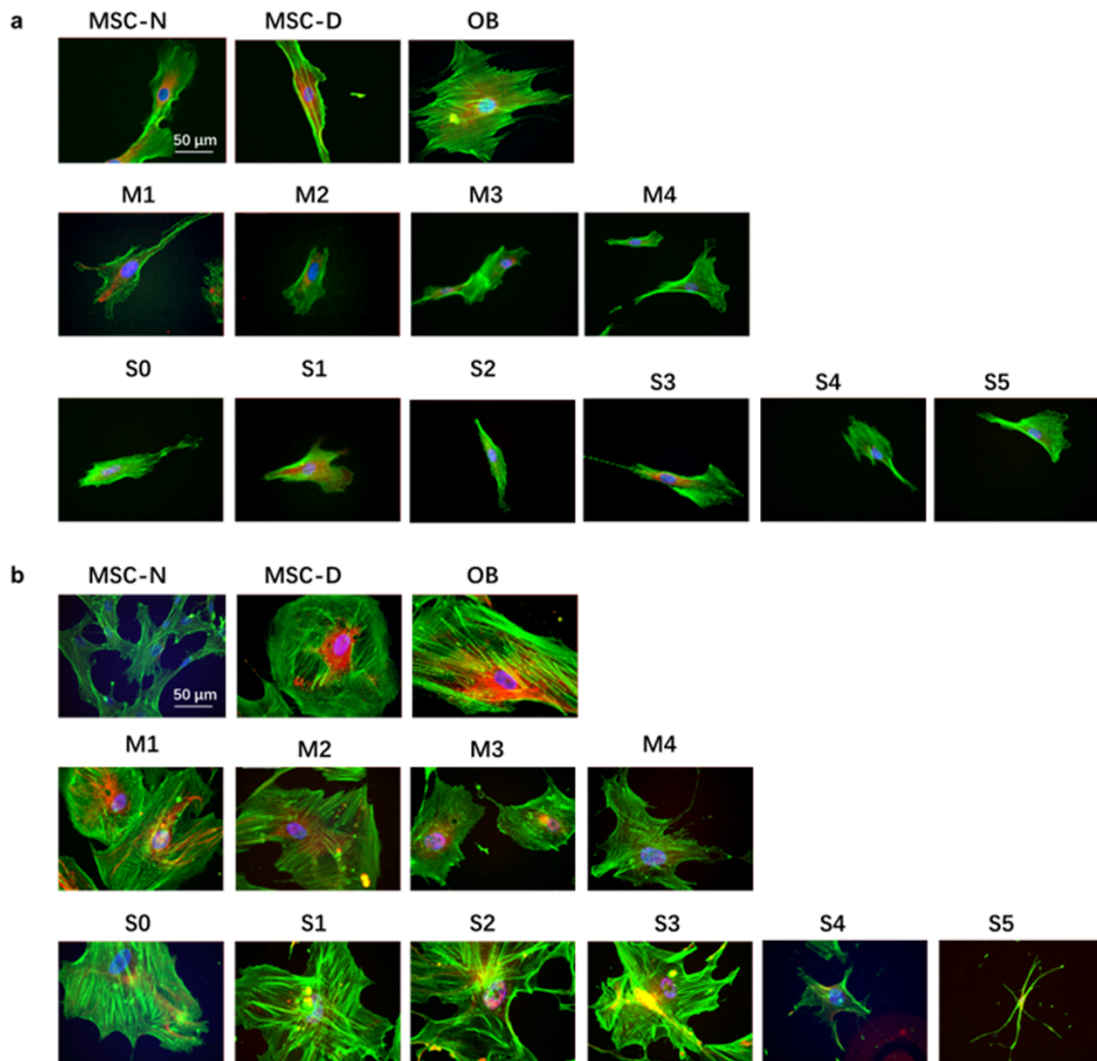


Fig. 6 Fluorescence images of hMSCs cultured for a) 24 h and b) 2W on the control group, the PET-MIX condition, and the PET-SPRAY condition. Cells were stained for the late osteogenic (OPN) marker in red, with F-actin stained in green and cell nucleus in blue. Objective 40x, scale bar: 50 μm.

As expected, culturing hMSCs for two weeks on uniformly peptide-functionalized surfaces (M1, M2, M3, and M4) resulted in a prevalent transition of cell shapes to cuboidal forms, a distinctive trait of osteoblasts (Fig. 6a and 6b). In contrast, cells grown on surfaces displaying disordered patterns (S0, S1, S2, S3, S4, S5) tended to adopt more columnar or cuboidal shapes. Notably, surfaces S4 and S5 displayed

dendrite-like star-shaped formations (Fig. 6a and 6b), resembling characteristics of osteocyte morphology.

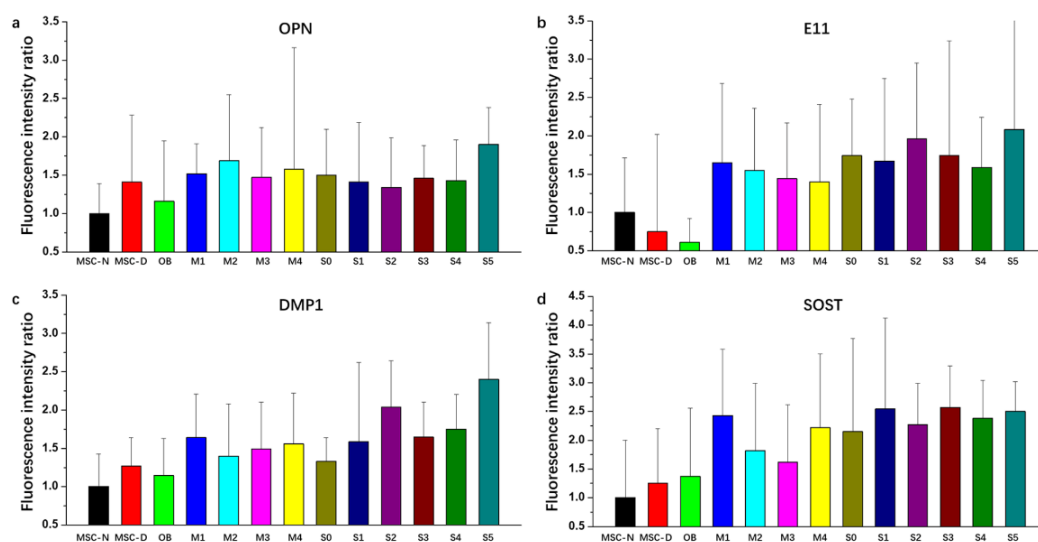


Fig. 7 Quantitative analysis of the immunofluorescence of a) OPN, b) E11, c) DMP1, d) SOST. The statistical analysis is presented in Supplementary Fig. S1, S2, S3, S4.

To precisely determine the commitment of hMSCs to the osteoblastic lineage, we conducted a comparative analysis of cell expression using various markers (as illustrated in Fig. 7). We quantified the intensity of osteopontin (OPN) expression, a marker associated with late-stage osteoblasts. The control group of MSC-N exhibited a significantly lower OPN expression compared to the M1, M2, M3, M4, S0, S1, S3, S4, and S5 groups. There is no significant difference of OPN expression between M1, M2, M3, and M4 groups. Moreover, there is no significant difference of OPN expression between S0, S1, S2, S3, and S4 groups. The distinguishing factor between these two conditions lies solely in the distribution pattern of peptides (Fig. 7, Fig S1, and Table 1).

The behavior of the S5 material is notably distinctive, showing a significant difference in OPN overexpression compared to OB, M1, M3, M4, S0, S1, S3, S4, and S5 material. (Fig. 7, Fig S1). Intriguingly, despite sharing an equivalent quantity of RGD and BMP-2 peptides with the M1 material, the S5 material exhibits a different micro-patterned surface with RGD + BMP-2 cues and BMP-2 distributed around (Table 1). Interestingly, we observed a consistent trend in the expression intensity of early osteocyte markers (DMP1 and E11) among cells, although not all the results showed significant differences: the disordered pattern group > the uniformly bioactive group > the control group (Fig. 7). Specifically, all spray materials, including S0, S1, S3, S4, and S5 material, demonstrated a significant increased intensity of E11 expression in cells after 2 weeks of culture compared to the control material MSC-N and MSC-D. Additionally, among all homogeneously bioactive materials (except M4) and PET-Spray surfaces, there was an elevated intensity of E11 expression compared to the MSC-D control. Both PET-MIX and PET-Spray materials exhibited an overexpression of E11 intensity compared to the OB condition (Fig. 7, Fig. S2). Interestingly, after 2 weeks of culture, cells on S2 showed elevated expression of E11 intensity when compared to M3, despite both having a similar surface quantity of RGD and BMP-2 peptides with only varied peptide distribution (Fig. 7, Fig. S2, and Table 1). Additionally, M3 and M4 demonstrated equivalent E11 intensities despite having entirely opposite peptide ratio distributions (88.5% RGD and 11.5% BMP-2 for M3; 11.5% RGD and 88.5% BMP-2 for M4) (Fig. 7, Fig. S2). The most remarkable E11 overexpression was observed in

cells on S5 compared to all other surfaces, except for S0, S2, and S3, where the results did not show significant differences (Fig. 7, Fig. S2).

In terms of DMP1 expression, after a 2-week culture period, all conditions (except S0) demonstrated an overexpression of DMP1 intensity compared to the MSC-N control (Fig. 7, Fig. S3). Only M1, S1, S2, S3, S4, and S5 showed a significantly different overexpression of DMP1 compared to MSC-D. For M1, S0, S1, S2, S3, S4, and S5, the DMP1 overexpression was notably distinct compared to the OB condition (Fig. 7, Fig. S3). S2 and S5 exhibited an increased expression of DMP1 when compared to M1, where the difference lay in the peptide distribution on the PET surface. Remarkably, akin to E11, S5 displayed an elevated DMP1 overexpression compared to all other conditions (PET-MIX, PET-Spray, and all controls) (Fig. 7, Fig. S3).

Finally, we evaluated the expression of the late osteocyte marker, SOST, in the cells. In the control group, there was generally low SOST expression. Conversely, within the PET-MIX condition, cells displayed increased SOST expression on M1, M2, M3, and M4 compared to the control group. Although there is a trend, not all results are considered significantly different (Fig. 7 and Fig. S4). However, the SOST expression levels among M1, M2, M3, and M4 did not exhibit significant variations. In the PET-Spray condition, one specific condition stood out prominently: S5. Cells on S5 notably exhibited the highest SOST expression with a lower error bar (indicating that more cells were at a similar stage of differentiation), which was significantly greater than in all other materials (Fig. 7 and Fig. S4).

Fig. S5 reveals that the expression of OPN in cells after 2 weeks is shifted towards higher intensities for the S5 material compared to M1 and the control groups (MSC-N, MSC-D and OB). M1 and S5 are two conditions with the same total amount of each peptide (RGD and BMP-2). The distribution is also larger in the case of S5. Fig. S6 undoubtedly confirms these observations as the expression of E11 is shifted towards higher intensities for the S5 and M1 materials compared to the control groups. Additionally, the number of cells expressing higher intensities of E11 is more significant for S5 than for M1 (75% and 62%, respectively). Fig. S7 clearly shows a difference between S5 and M1 and the two control conditions. The distribution is broader for S5, indicating that cells exhibit an overexpression of DMP1 with the S5 condition.

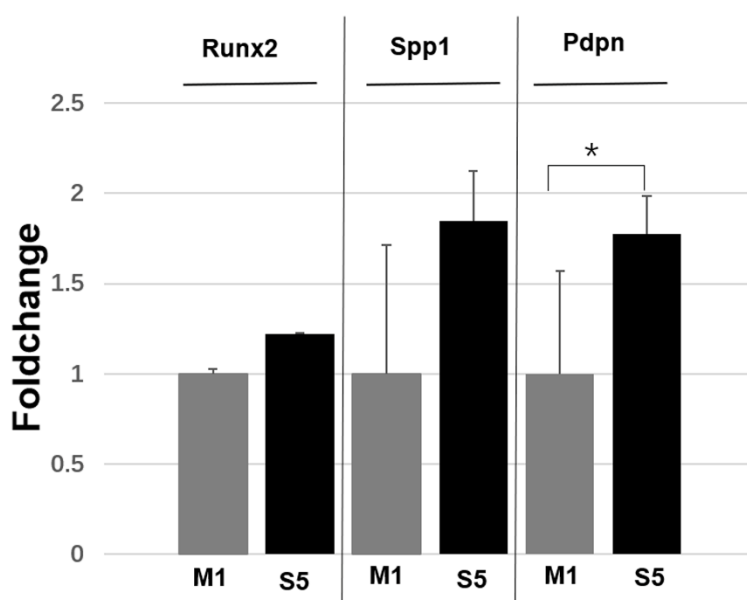


Fig. 8: RT-qPCR analysis of the expression levels of the osteogenesis-related genes of Runx2, Spp1 and Pdpn in two groups (M1 and S5) after 2 weeks of culture.

q-PCR analysis. The qPCR analysis aimed to assess the expression of Runx2, Spp1, and Pdpn in hMSCs cultured for 2 weeks under conditions M1 and S5. According to the qPCR results (Fig. 8), the surface that most effectively prompted osteogenic differentiation of hMSCs was the S5 condition. We notice a consistent trend of increase in the expression of all three genes, although the increase in Runx2 and Spp1 is not statistically significant. Interestingly, we distinctly observe a significant increase in Pdpn expression, which is an early marker for osteocyte differentiation.

Cell shape. To analyze how different disordered bioactive micro- and nanopatterns affect the cellular behavior of hMSCs, we evaluated the cell shapes on different samples after 2 weeks of culture by calculating morphometric parameters, including aspect ratio, circularity, and anisotropy.

Aspect ratio is defined as the major axis/minor axis. It means that the more elongated shape, the greater aspect ratio value. Circularity is defined as $4\pi \times \text{cell area}/\text{perimeter}^2$. The increase in cell circularity indicates a shift in cell shape from being round with numerous protrusions to having fewer protrusions. In other word, a high cell circularity value indicates a low degree of cell protrusion. In addition, the anisotropy parameter can evaluate the degree of orientation of f-actin via the FibrilTool plugin.³⁵ The anisotropy parameter value is in the interval 0-1. Furthermore, 0 corresponds to disordered f-actin (purely isotropic fibres), and 1 indicates that f-actin is perfectly ordered (parallel fibres). It means that the lower the anisotropy parameter value, the more disordered the distribution of F-actin within the cell.¹⁶

Fig. S8 illustrates the cell aspect ratio results following a two-week culture on various samples. Initially, notable differences were observed between the two control groups (MSC-N and OB). In MSC-N, cell aspect ratio values were predominantly concentrated within the 1-3.5 range, maintaining consistent values across intervals. Conversely, the OB group primarily exhibited cell aspect ratio values within the 1-2 interval, indicating a lower aspect ratio and fewer elongated cells compared to MSC-N. Following a two-week culture on M1 and S5, the distribution of cell aspect ratios closely resembled that of the OB group. Interestingly, in these two groups, there was a higher proportion of cell aspect ratios within the 1.5-2 interval compared to the OB group, while the proportion within the 1-1.5 interval was lower than that of the OB group.

Fig. S9 displays the cell circularity results across various conditions after 2 weeks of cell culture. In the MSC-N group, cell circularity values exhibited a fan-shaped distribution trend within the 0-0.8 range, primarily concentrating around 0.3-0.5. Conversely, within the OB group, cell circularity values were primarily concentrated within 0.6-0.9, with a smaller number clustered around 0-0.3. This suggests that most cells in the OB group displayed higher circularity, consistent with the typical cubic shape of osteoblasts. Conventionally, osteocytes exhibit a star-shaped morphology, characterized by lower circularity values. Notably, cell circularity values of those cultured in S5 were concentrated within the 0-0.3 range, particularly notable in the distribution intervals of 0-0.1, 0.1-0.2, and 0.2-0.3, accounting for 8%, 28%, and 23%, respectively.

Fig. S10 illustrates the anisotropy results of cells cultured on various samples for 2 weeks. In the MSC-N group, there is an observable increasing trend in the distribution of anisotropy values, indicating a parallel trend in intracellular F-actin alignment. Cells in the OB group primarily exhibited anisotropy values concentrated within the range of 0.2-0.5. Conversely, the remaining two groups showed cell anisotropy values concentrated within the 0-0.3 range. Particularly, cells cultured on S5 displayed the highest proportion of anisotropy values within the 0-0.1 range, suggesting the highest degree of disordered F-actin among the groups.

DISCUSSION

The development of bone tissue engineering offers new prospects for treating bone defects and advancing regenerative medicine. Stem cells, known for their unique self-renewal and differentiation capabilities, are at the forefront of research interest. However, a significant challenge in the field remains the precise control over stem cell growth and differentiation.^{38,39} The cellular behavior is profoundly influenced by the multifaceted extracellular matrix (ECM) environment, encompassing factors such as ECM protein concentration and various stimuli from the stem cell niche. These stimuli include both chemical cues,^{16,17,40-45} such as composition^{16,17,30,40,41,46-48} and ligand density, and physical factors like matrix stiffness,⁴⁹⁻⁵¹ surface topography,^{48,52,53} and interfacial hydrophobicity.⁵⁴ An ideal approach would involve replicating key ECM attributes while structuring instructional cues to guide cellular responses. In vivo, cells

interact with specific peptide motifs within the ECM, primarily through receptors like integrins, as the ECM is rich in proteins such as collagen, laminin, and fibronectin.⁵⁵

⁵⁶ Peptides, due to their advantageous properties, are increasingly utilized to modify biomaterials, offering simplicity, cost-effectiveness, and resistance to environmental conditions.^{55, 56} Various peptides mimicking ECM proteins and growth factors have been identified, including the significant biomaterial bioactive factor, RGD (Arg-Gly-Asp). RGD peptides, abundant in ECM proteins, serve as anchoring sites for integrin receptors, promoting cell adhesion and proliferation.⁵⁵⁻⁵⁷ The combination of peptides with materials enriches biomaterials with specific sequences that encourage cell adhesion or trigger cell signaling pathways. Peptides derived from the transforming growth factor beta family (TGF- β), such as BMP-2, have been utilized alone or in combination with adhesion peptides to induce cell differentiation.^{16, 17, 30, 40, 41, 44-48, 58,}

⁵⁹ Despite the emphasis on this synergistic effect in numerous studies, contradictory findings exist in the scientific literature.⁶⁰ The results reported by Bilem et al.¹⁵ have highlighted the notable influence of the co-presence of RGD and BMP-2 mimetic peptides, with densities of 0.7 pmol/mm² and 1 pmol/mm² respectively, on the expression of osteogenic markers. This resulted in a twofold increase in the Runx-2 level compared to surfaces containing only BMP-2 mimetic peptides. The upregulation of Runx-2 expression strongly indicates a shift of hMSCs toward the osteoblast lineage. It suggests that RGD and BMP-2 mimetic peptides synergistically accelerate hMSCs' commitment to osteogenesis. This synergistic effect has been previously observed by He et al. in their study on rat BMSCs cultured on hydrogels functionalized with RGD

+ BMP-2 mimetic peptides.⁶¹ Their hypothesis was that the RGD peptide provides attachment sites for cells on the substrates, facilitating the interaction of BMP-2 mimetic peptides with their transmembrane receptors, BMPR I and BMPR II, thus enhancing osteogenesis. This assumption seems reasonable considering Lai and Cheng's results that BMP-2 receptors co-localize with α_v and β_1 integrin subunits at focal adhesion points, facilitating the interaction between BMP-2 receptors and their ligands within the ECM.⁶² Moreover, integrin signaling plays a vital role in BMP-2 receptor activation. For example, blocking $\alpha_v\beta$ integrins using α_v integrin antibodies suppressed Smad signaling triggered by BMP-2 receptor activation.⁶³ This implies that the osteogenic effect of BMP-2 mimetic peptides depends not only on BMP-2 receptor activation, as suggested in previous works, but also on integrin signaling. Suzawa et al. added more insight into the cooperation mechanism between RGD and BMP-2 mimetic peptides.⁶⁴ They demonstrated that Ras-ERK signals enhance BMP-2 bioactivity by directly influencing Smad 1 transcriptional activity, with Ras-ERK potentially being downstream signals of activated $\alpha_2\beta_1$ -integrin. For instance, Kim et al.⁶⁵ modified tissue culture polystyrene (TCP) surfaces with BMP-2, RGD + BMP-2, or scrambled (sc) RGD + BMP-2 peptides, using sc-RGD as a negative control for RGD. However, on RGD + BMP-2 surfaces with the same BMP-2 density as sc-RGD + BMP-2 surfaces, the osteogenic effect of BMP-2 peptides was notably reduced, leading to a downregulation of Alkaline Phosphatase (ALP) activity and calcium deposition compared to BMP-2 and sc-RGD + BMP-2 surfaces. This discrepancy between the effects of RGD peptides on stem cells and progenitor response to BMP-2 peptides, as

reported by Kim et al.⁶⁵ and Koepsel et al.⁶⁰ may stem from differing peptide densities that significantly impact cell behavior, the method of peptide attachment to the biomaterial, as well as the medium conditions used for biological experiments.

Overall, our results emphasize that the combination of RGD and BMP-2 mimetic peptides synergistically promotes osteogenic differentiation of hMSCs, whether on uniformly functionalized surfaces or with micropatterns. It is important to note that the S5 condition exhibits cells resembling osteocytes, an overexpression of late osteoblastic markers, as well as early and late osteocyte markers, along with micropatterns containing both RGD and BMP-2 peptides. The second condition that significantly promotes both osteoblastic and osteocyte differentiation is the M1 condition, which has equal quantities of RGD and BMP-2. Ultimately, at equivalent peptide densities for each peptide, the disordered distribution in the form of micropatterns appears to be the most effective.

In vitro, numerous reports have demonstrated that topographical, physical or biochemical features affect stem cell behavior, including adhesion, proliferation, and changes in cytoskeleton conformation.^{48, 65} Currently, researchers have developed many techniques for creating micro- or nano-topography. Common techniques include photolithography, electron beam lithography, dip pen nanolithography, and so on.^{12, 66-68} Very few publications have been found in the literature regarding the use of the spray technique for the preparation of micropatterned surfaces.^{25, 26} This should change considering the growing interest in synthesizing disordered micro-, nanopatterned surfaces : indeed, a novel concept was introduced by Dalby et al.,¹⁸ who utilized

electron beam lithography (EBL) to create nanotopographies with varying degrees of symmetry and disorder on the PMMA surface. They subsequently investigated how osteoprogenitor and mesenchymal stem cells responded to these nanoscale features.¹⁸ The study demonstrated that highly ordered nano-topologies had minimal impact on cell adhesion and osteoblast differentiation. In contrast, cells encountering random nano-cues displayed more osteoblastic morphology after a 14-day period. Following 21 days of cell culture, MSCs on the surface featuring random nanopits (arranged in a randomized pattern on a $150\ \mu\text{m} \times 150\ \mu\text{m}$ area and uniformly distributed over a $1\ \text{cm}^2$ area) exhibited a more typical polygonal osteocyte morphology. Furthermore, research findings have indicated that ordered nanopits may lead to reduced cell adhesion.⁶⁹ On the other hand, disordered nanopits have been shown to better facilitate bone formation.⁷⁰ Bilem *et al.* reported decorating glass surfaces with subcellular patterns of RGD and BMP-2 ligands by using photolithography. Their results demonstrate that ordered geometric cues guide stem cell differentiation in a ligand-type-dependent manner.^{15, 17, 40} All of these studies employed the photolithography technique to create ordered bioactive micropatterns with various geometries on the surface. It's worth noting that the uniqueness of our research lies in the development of disordered bioactive patterns on polymer surfaces through a cost-effective approach. Laroche's team used a spray technique for micropatterned surface to support cell growth. This technology is based on the stochastic nature of aerosols and the principle of liquid atomization.^{25, 26} The authors highlighted that in comparison with other patterning methods, this technique offers the advantages of rapid operation, ease of use, and

affordability. Their team employed this technique to generate disordered patterns on polytetrafluoroethylene (PTFE) surfaces by covalently grafting CGRGDS and CWQPPRARI peptides. They subsequently evaluated the impact of these patterns on the behavior of bovine aortic endothelial cells (BAECs). The team observed that CGRGDS spots, with a diameter of 10 ± 2 μm against a background of CWQPPRARI peptides, exhibited the highest potential for enhancing endothelialization.

In a previous study conducted by our team, employing the same Spray methodology, we demonstrated that the distribution of BMP-2 peptide micropatterns influence the fate of hMSCs²⁹. In our current study, we established four PET-Spray conditions with identical peptide surface coverage as our previous publication²⁹ (23% for sprayed peptide and 77% for solution-immobilized peptide on untreated PET surfaces), but varying peptide compositions. S0 contained 23% RGD (sprayed) and 77% BMP-2, while S1 comprised 23% BMP-2 (sprayed) and 77% RGD. S2 and S4 both featured a blend of 23% BMP-2 + RGD within micropatterns, with S2 having 77% RGD and S4 having 77% BMP-2 in total. Additionally, we introduced two conditions with distinct micropattern size distributions: S3 and S5. S3 incorporated 50% BMP-2 + RGD within micropatterns and 50% RGD on untreated PET surfaces, while S5 featured 50% BMP-2 + RGD within micropatterns and 50% BMP-2 on untreated surfaces. To compare disordered patterns versus homogeneous bioactive surfaces on cell behavior at equivalent peptide content, we prepared a series of homogeneous bioactive surfaces (M1, M2, M3, M4). M1 and M2 (as well as M3 and M4) had opposing percentages of each RGD and BMP-2 peptide on the surface. Peptide density on PET surfaces, both

alone and dual-functionalized with fluorescent peptides, was assessed via fluorescence microscopy. Interestingly, these results were consistent with the theoretical predictions. Immunocytochemistry and qPCR revealed enhanced expression of osteoblast and osteocyte markers on PET-Spray surfaces, particularly on S5 compared to PET-MIX surfaces. When cells were cultured on PET-MIX surfaces, significant differences were observed only between M1 and M3 in SOST expression intensity. When cells were cultured in the PET-Spray group, higher expression of E11 and DMP1 was observed on S2 and S5. Regarding the intensity of OPN expression, although not all differences are statistically significant between the various conditions, all materials from the PET-Spray group exhibited lower error bars. This point should be taken into consideration as it indicates a larger number of cells being at the same differentiation stage. S2 and S5 present a different distribution of micropattern sizes. The size distribution of micropatterns is narrower for materials S0, S1, S2, and S4 compared to materials S3 and S5. The expression levels of DMP1, E11, and SOST in S5 were significantly higher than those in S2, indicating that not only a surface with a higher concentration of BMPs, but also a broader distribution of micropatterns had a greater potential to induce cells to differentiate into the osteoblast and osteocyte lineages. Overall, S5 exhibited the highest expression levels of osteoblast and osteocyte markers, indicating its potential to induce cell differentiation. Additionally, Phalloidin staining showed dendritic cell presence on S5, characteristic of osteocytes.

As far as we know, the in vitro differentiation of hMSCs into osteocytes in 2D is rarely reported in the literature^{27, 63, 64} because the transition from osteoblasts to osteocytes

necessitates a 3D environment.²⁷ Our work highlighted that the selection of peptides for immobilization and their distribution on the surface guide the differentiation of hMSCs toward osteocyte differentiation. Our future experiments will focus on two main axes: the immobilization of multifunctional peptides and the design of 3D scaffolds using hydrogels through bioprinting, incorporating this spray system to treat each layer.

CONCLUSIONS

We present a novel sequential 2D culture system for efficiently generating abundant bone cells (osteoblasts, osteocytes). Our study introduces the application of spray technology to synthesize disordered bioactive micro/nanopatterned surfaces, shedding light on their impact on hMSC differentiation. To compare the effects of disordered patterns versus homogeneous bioactive surfaces on cell behavior at equivalent peptide content, we prepared a series of homogeneous bioactive surfaces (M1-M4) with uniform peptide distribution. These were compared with micropatterned surfaces (S0-S5) featuring varying ratios of RGD and BMP-2 peptides. We assessed hMSC differentiation towards the bone lineage through immunocytochemistry and qPCR analysis, as well as analyzing cell shape using anisotropy and circularity analyses. The S5 condition, displaying micropatterns of both RGD and BMP-2 peptides, promoted osteocyte-like cell morphology and overexpression of osteoblastic and osteocyte markers. Our findings underscore the synergistic effect of combining RGD and BMP-2 peptides within micropatterns to enhance hMSC osteogenic differentiation. Notably, the spraying technique allows for the consistent production of varied micropattern size distributions, facilitating the exploration of their impact on hMSC differentiation. This

study represents a pioneering approach to in vitro differentiation of hMSCs into osteocytes using 2D surfaces, advancing our understanding of hMSC osteogenic differentiation and osteocyte functionality in bone biology. Moreover, our spraying protocol is easily scalable for large-scale manufacturing, offering precise control over stem cell behavior on various disordered bioactive micro/nanopatterns.

ASSOCIATED CONTENT

Supporting Information

Statistical analysis and Class distribution of OPN, E11, DMP1, SOST after 2 weeks of culture. Class distribution of cell shapes, including aspect ratio, circularity and anisotropy value after 2W. The Supporting Information is available free of charge. (PDF)

AUTHOR INFORMATION

Authors

Yujie ZHANG – *Univ. Bordeaux, CNRS, Bordeaux INP, CBMN, UMR 5248, France*

Murielle REMY – *Univ. Bordeaux, CNRS, Bordeaux INP, CBMN, UMR 5248, France*

Thierry LESTE-LASSERRE – *Univ. Bordeaux, INSERM, PUMA, Neurocentre Magendie, U1215, Bordeaux, France*

Marie-Christine DURRIEU – *Univ. Bordeaux, CNRS, Bordeaux INP, CBMN, UMR 5248, France*

Author Contributions

Yujie Zhang: conceptualization, validation, formal analysis, investigation, writing – original draft, and visualization. Murielle Remy: methodology (Supervision in cell culture experiments). Thierry Leste-Lasserre: methodology (qPCR analysis). Marie-Christine Durrieu: conceptualization, validation, writing & editing, supervision, and funding acquisition. All authors have given approval to the final version of the manuscript.

Notes

The authors declare no competing financial interest.

ACKNOWLEDGEMENTS

The authors thank Professor Gaetan Laroche from Laval University for his help for the design of the spray technique. This work was supported by the French “Agence Nationale de la Recherche” (ANR-21-CE06-0031-02) (M.C.D.). The financial the financial support from China Scholarship Council (CSC) is also acknowledged.

REFERENCES

1. Tsiapalis, D.; O'Driscoll, L., Mesenchymal stem cell derived extracellular vesicles for tissue engineering and regenerative medicine applications. *Cells* **2020**, *9* (4), 991.
2. Stammitz, S.; Klimczak, A., Mesenchymal Stem Cells, Bioactive Factors, and Scaffolds in Bone Repair: From Research Perspectives to Clinical Practice. *Cells* **2021**, *10* (8), 1925.
3. Bianco, P.; Robey, P. G., Stem cells in tissue engineering. *Nature* **2001**, *414* (6859), 118-21.
4. Oreffo, R. O.; Cooper, C.; Mason, C.; Clements, M., Mesenchymal stem cells: lineage, plasticity, and skeletal therapeutic potential. *Stem Cell Rev.* **2005**, *1* (2), 169-78.
5. Kanchanawong, P.; Calderwood, D. A., Organization, dynamics and mechanoregulation of integrin-mediated cell–ECM adhesions. *Nat. Rev. Mol. Cell Biol.* **2023**, *24* (2), 142-161.
6. Hou, Y.; Xie, W.; Yu, L.; Camacho, L. C.; Nie, C.; Zhang, M.; Haag, R.; Wei, Q., Surface Roughness Gradients Reveal Topography-Specific Mechanosensitive Responses in Human Mesenchymal Stem Cells. *Small* **2020**, *16* (10), 1905422.
7. Esfahani, S. N.; Irizarry, A. M. R.; Xue, X.; Lee, S. B.-D.; Shao, Y.; Fu, J., Micro/nanoengineered technologies for human pluripotent stem cells maintenance and differentiation. *Nano Today* **2021**, *41*, 101310.
8. Luo, J.; Walker, M.; Xiao, Y.; Donnelly, H.; Dalby, M. J.; Salmeron-Sanchez, M., The influence of nanotopography on cell behaviour through interactions with the extracellular matrix—a review. *Bioact. Mater.* **2022**, *15*, 145-159.
9. Sousa, M. P.; Arab-Tehrany, E.; Cleymand, F.; Mano, J. F., Surface Micro-and Nanoengineering: Applications of Layer-by-Layer Technology as a Versatile Tool to Control Cellular Behavior. *Small* **2019**, *15* (30), 1901228.
10. Eftekhari, B. S.; Eskandari, M.; Janmey, P. A.; Samadikuchaksaraei, A.; Gholipourmalekabadi, M., Surface Topography and Electrical Signaling: Single and Synergistic Effects on Neural Differentiation of Stem Cells. *Adv. Funct. Mater.* **2020**, *30* (25), 1907792.
11. Ron, A.; Azeloglu, E. U.; Calizo, R. C.; Hu, M.; Bhattacharya, S.; Chen, Y.; Jayaraman, G.; Lee, S.; Neves-Zaph, S. R.; Li, H., Cell shape information is transduced through tension-independent mechanisms. *Nat. Commun.* **2017**, *8* (1), 2145.
12. Liu, G.; Petrosko, S. H.; Zheng, Z.; Mirkin, C. A., Evolution of dip-pen nanolithography (DPN): From molecular patterning to materials discovery. *Chem. Rev.* **2020**, *120* (13), 6009-6047.
13. Carthew, J.; Taylor, J. B. J.; Garcia-Cruz, M. R.; Kiaie, N.; Voelcker, N. H.; Cadarso, V. J.; Frith, J. E., The Bumpy Road to Stem Cell Therapies: Rational Design of Surface Topographies to Dictate Stem Cell Mechanotransduction and Fate. *ACS Appl. Mater. Interfaces* **2022**, *14* (20), 23066-23101.
14. Giam, L. R.; Massich, M. D.; Hao, L.; Shin Wong, L.; Mader, C. C.; Mirkin, C. A., Scanning probe-enabled nanocombinatorics define the relationship between fibronectin feature size and stem cell fate. *Proc. Natl. Acad. Sci.* **2012**, *109* (12), 4377-4382.
15. Bilem, I.; Chevallier, P.; Plawinski, L.; Sone, E.; Durrieu, M.; Laroche, G., RGD and BMP-2 mimetic peptide crosstalk enhances osteogenic commitment of human bone marrow stem cells. *Acta Biomater.* **2016**, *36*, 132-142.

16. Bilem, I.; Chevallier, P.; Plawinski, L.; Sone, E. D.; Durrieu, M.-C.; Laroche, G., Interplay of Geometric Cues and RGD/BMP-2 Crosstalk in Directing Stem Cell Fate. *ACS Biomater. Sci. Eng.* **2017**, *3* (10), 2514-2523.
17. Padiolleau, L.; Chanseau, C.; Durrieu, S.; Chevallier, P.; Laroche, G.; Durrieu, M.-C., Single or Mixed Tethered Peptides To Promote hMSC Differentiation toward Osteoblastic Lineage. *ACS Appl. Bio Mater.* **2018**, *1* (6), 1800-1809.
18. Dalby, M. J.; Gadegaard, N.; Tare, R.; Andar, A.; Riehle, M. O.; Herzyk, P.; Wilkinson, C. D. W.; Oreffo, R. O. C., The control of human mesenchymal cell differentiation using nanoscale symmetry and disorder. *Nat. Mater.* **2007**, *6* (12), 997-1003.
19. Decker, D.; Hempelmann, R.; Natter, H.; Pirrung, M.; Rabe, H.; Schäfer, K. H.; Saumer, M., 3D nanostructured multielectrode arrays: fabrication, electrochemical characterization, and evaluation of cell–electrode adhesion. *Adv. Mater. Technol.* **2019**, *4* (2), 1800436.
20. Wang, L.-S.; Duncan, B.; Tang, R.; Lee, Y.-W.; Creran, B.; Elci, S. G.; Zhu, J.; Yesilbag Tonga, G. I.; Doble, J.; Fessenden, M., Gradient and patterned protein films stabilized via nanoimprint lithography for engineered interactions with cells. *ACS Appl. Mater. Interfaces* **2017**, *9* (1), 42-46.
21. Yang, K.; Jung, K.; Ko, E.; Kim, J.; Park, K. I.; Kim, J.; Cho, S. W., Nanotopographical manipulation of focal adhesion formation for enhanced differentiation of human neural stem cells. *ACS Appl. Mater. Interfaces* **2013**, *5* (21), 10529-40.
22. Yim, E. K.; Pang, S. W.; Leong, K. W., Synthetic nanostructures inducing differentiation of human mesenchymal stem cells into neuronal lineage. *Exp. Cell Res.* **2007**, *313* (9), 1820-9.
23. Celik, N.; Torun, I.; Ruzi, M.; Esidir, A.; Onses, M. S., Fabrication of robust superhydrophobic surfaces by one-step spray coating: Evaporation driven self-assembly of wax and nanoparticles into hierarchical structures. *Chem. Eng. J.* **2020**, *396*, 125230.
24. Guo, R.; Goudeli, E.; Xu, W.; Richardson, J. J.; Xu, W.; Pan, S., Exploiting Molecular Dynamics in Composite Coatings to Design Robust Super-Repellent Surfaces. *Adv. Sci. (Weinh)* **2022**, *9* (6), e2104331.
25. Gagne, L.; Laroche, G., Engineering Biomaterials Surfaces Using Micropatterning. *Adv. Mater. Res.* **2007**, *15-17*, 77-82.
26. Gagné, L.; Rivera, G.; Laroche, G., Micropatterning with aerosols: application for biomaterials. *Biomaterials* **2006**, *27* (31), 5430-5439.
27. Skottke, J.; Gelinsky, M.; Bernhardt, A., In Vitro Co-culture Model of Primary Human Osteoblasts and Osteocytes in Collagen Gels. *Int. J. Mol. Sci.* **2019**, *20* (8).
28. Chollet, C.; Chanseau, C.; Remy, M.; Guignandon, A.; Bareille, R.; Labrugère, C.; Bordenave, L.; Durrieu, M. C., The effect of RGD density on osteoblast and endothelial cell behavior on RGD-grafted polyethylene terephthalate surfaces. *Biomaterials* **2009**, *30* (5), 711-20.
29. Zouani, O. F.; Chollet, C.; Guillotin, B.; Durrieu, M. C., Differentiation of pre-osteoblast cells on poly(ethylene terephthalate) grafted with RGD and/or BMPs mimetic peptides. *Biomaterials* **2010**, *31* (32), 8245-53.
30. Zouani, O. F.; Chanseau, C.; Brouillaud, B.; Bareille, R.; Deliane, F.; Foulc, M.-P.; Mehdi, A.; Durrieu, M.-C., Altered nanofeature size dictates stem cell differentiation. *J. Cell Sci.* **2012**, *125* (5), 1217-1224.
31. Chen, Y. W.; Huang, H. S.; Shieh, Y. S.; Ma, K. H.; Huang, S. H.; Hueng, D. Y.; Sytwu, H. K.; Lin, G. J., A novel compound NSC745885 exerts an anti-tumor effect on tongue cancer SAS cells in vitro and in vivo. *PLoS One* **2014**, *9* (8), e104703.

32. Zhang, Y.; Rémy, M.; Apartsin, E.; Prouvé, E.; Feuillie, C.; Labrugère, C.; Cam, N.; Durrieu, M.-C., Controlling differentiation of stem cells via bioactive disordered cues. *Biomater. Sci.* **2023**, *11* (18), 6116-6134.
33. Gillman, C. E.; Jayasuriya, A. C., FDA-approved bone grafts and bone graft substitute devices in bone regeneration. *Mater. Sci. Eng. C* **2021**, *130*, 112466.
34. Huang, B.; Yuan, Y.; Liu, C., Biomaterial-guided immobilization and osteoactivity of bone morphogenetic protein-2. *Applied Materials Today* **2020**, *19*, 100599.
35. Boudaoud, A.; Burian, A.; Borowska-Wykręt, D.; Uyttewaal, M.; Wrzalik, R.; Kwiatkowska, D.; Hamant, O., FibrilTool, an ImageJ plug-in to quantify fibrillar structures in raw microscopy images. *Nat. Protoc.* **2014**, *9* (2), 457-463.
36. Bustin, S. A.; Benes, V.; Garson, J. A.; Hellemans, J.; Huggett, J.; Kubista, M.; Mueller, R.; Nolan, T.; Pfaffl, M. W.; Shipley, G. L.; Vandesompele, J.; Wittwer, C. T., The MIQE guidelines: minimum information for publication of quantitative real-time PCR experiments. *Clin. Chem.* **2009**, *55* (4), 611-22.
37. Xie, F.; Xiao, P.; Chen, D.; Xu, L.; Zhang, B., miRDeepFinder: a miRNA analysis tool for deep sequencing of plant small RNAs. *Plant Mol. Biol.* **2012**, *80* (1):75–84.
38. Watt, F. M.; Huck, W. T. S., Role of the extracellular matrix in regulating stem cell fate. *Nat. Rev. Mol. Cell Biol.* **2013**, *14* (8), 467-473.
39. Gultian, K. A.; Gandhi, R.; Sarin, K.; Sladkova-Faure, M.; Zimmer, M.; de Peppo, G. M.; Vega, S. L., Human induced mesenchymal stem cells display increased sensitivity to matrix stiffness. *Sci. Rep.* **2022**, *12* (1), 8483.
40. Bilem, I.; Plawinski, L.; Chevallier, P.; Ayela, C.; Sone, E. D.; Laroche, G.; Durrieu, M. C., The spatial patterning of RGD and BMP-2 mimetic peptides at the subcellular scale modulates human mesenchymal stem cells osteogenesis. *J. Biomed. Mater. Res., Part A* **2018**, *106* (4), 959-970.
41. Cheng, Z. A.; Zouani, O. F.; Glinel, K.; Jonas, A. M.; Durrieu, M.-C., Bioactive Chemical Nanopatterns Impact Human Mesenchymal Stem Cell Fate. *Nano Lett.* **2013**, *13* (8), 3923-3929.
42. Nishida, K.; Baba, K.; Murakami, D.; Tanaka, M., Nanoscopic analyses of cell-adhesive protein adsorption on poly(2-methoxyethyl acrylate) surfaces. *Biomater. Sci.* **2022**, *10* (11), 2953-2963.
43. Stevens, M. M.; George, J. H., Exploring and engineering the cell surface interface. *Science* **2005**, *310* (5751), 1135-1138.
44. Gaharwar, A. K.; Avery, R. K.; Assmann, A.; Paul, A.; McKinley, G. H.; Khademhosseini, A.; Olsen, B. D., Shear-Thinning Nanocomposite Hydrogels for the Treatment of Hemorrhage. *ACS Nano* **2014**, *8* (10), 9833-9842.
45. Royer, C.; Bégin, A.-A. G.; Plawinski, L.; Lévesque, L.; Durrieu, M.-C.; Laroche, G., Validation of reference genes for real-time PCR of cord blood mononuclear cells, differentiating endothelial progenitor cells, and mature endothelial cells. *Exp. Cell Res.* **2018**, *370* (2), 389-398.
46. Lei, Y.; Zouani, O. F.; Remy, M.; Ayela, C.; Durrieu, M.-C., Geometrical Microfeature Cues for Directing Tubulogenesis of Endothelial Cells. *PLoS ONE* **2012**, *7* (7), e41163.
47. Benoit, D. S. W.; Schwartz, M. P.; Durney, A. R.; Anseth, K. S., Small functional groups for controlled differentiation of hydrogel-encapsulated human mesenchymal stem cells. *Nat. Mater.* **2008**, *7* (10), 816-823.
48. Das, R. K.; Zouani, O. F.; Labrugère, C.; Oda, R.; Durrieu, M.-C., Influence of nanohelical shape and periodicity on stem cell fate. *ACS Nano* **2013**, *7* (4), 3351-3361.

49. Discher, D. E.; Mooney, D. J.; Zandstra, P. W., Growth factors, matrices, and forces combine and control stem cells. *Science* **2009**, *324* (5935), 1673-1677.
50. Fu, J.; Wang, Y.-K.; Yang, M. T.; Desai, R. A.; Yu, X.; Liu, Z.; Chen, C. S., Mechanical regulation of cell function with geometrically modulated elastomeric substrates. *Nat. Methods* **2010**, *7* (9), 733-736.
51. Prouvé, E.; Drouin, B.; Chevallier, P.; Rémy, M.; Durrieu, M.-C.; Laroche, G., Evaluating Poly(Acrylamide-co-Acrylic Acid) Hydrogels Stress Relaxation to Direct the Osteogenic Differentiation of Mesenchymal Stem Cells. *Macromol. Biosci.* **2021**, *21* (6), 2100069.
52. Pedrosa, C. R.; Arl, D.; Gysan, P.; Khan, I.; Durrieu, S.; Krishnamoorthy, S.; Durrieu, M.-C., Controlled Nanoscale Topographies for Osteogenic Differentiation of Mesenchymal Stem Cells. *ACS Appl. Mater. Interfaces* **2019**, *11* (9), 8858-8866.
53. Cunha, A.; Zouani, O. F.; Plawinski, L.; Botelho do Rego, A. M.; Almeida, A.; Vilar, R.; Durrieu, M.-C., Human mesenchymal stem cell behavior on femtosecond laser-textured Ti-6Al-4V surfaces. *Nanomedicine* **2015**, *10* (5), 725-739.
54. Ayala, R.; Zhang, C.; Yang, D.; Hwang, Y.; Aung, A.; Shroff, S. S.; Arce, F. T.; Lal, R.; Arya, G.; Varghese, S., Engineering the cell-material interface for controlling stem cell adhesion, migration, and differentiation. *Biomaterials* **2011**, *32* (15), 3700-3711.
55. Hosoyama, K.; Lazurko, C.; Muñoz, M.; McTiernan, C. D.; Alarcon, E. I., Peptide-based functional biomaterials for soft-tissue repair. *Front. Bioeng. Biotech.* **2019**, *7* (205), 1-19
56. Klimek, K.; Ginalska, G., Proteins and peptides as important modifiers of the polymer scaffolds for tissue engineering applications—a review. *Polymers* **2020**, *12* (4), 844.
57. Pountos, I.; Panteli, M.; Lampropoulos, A.; Jones, E.; Calori, G. M.; Giannoudis, P. V., The role of peptides in bone healing and regeneration: a systematic review. *BMC Med.* **2016**, *14*, 1-15.
58. Zouani, O. F.; Kalisky, J.; Ibarboure, E.; Durrieu, M.-C., Effect of BMP-2 from matrices of different stiffnesses for the modulation of stem cell fate. *Biomaterials* **2013**, *34* (9), 2157-2166.
59. Yao, X.; Hu, Y.; Cao, B.; Peng, R.; Ding, J., Effects of surface molecular chirality on adhesion and differentiation of stem cells. *Biomaterials* **2013**, *34* (36), 9001-9.
60. Koepsel, J. T.; Brown, P. T.; Loveland, S. G.; Li, W.-J.; Murphy, W. L., Combinatorial screening of chemically defined human mesenchymal stem cell culture substrates. *J. Mater. Chem.* **2012**, *22* (37), 19474-19481.
61. He, X.; Ma, J.; Jabbari, E., Effect of Grafting RGD and BMP-2 Protein-Derived Peptides to a Hydrogel Substrate on Osteogenic Differentiation of Marrow Stromal Cells. *Langmuir* **2008**, *24* (21), 12508-12516.
62. Lai, C. F.; Cheng, S. L., Alphavbeta integrins play an essential role in BMP-2 induction of osteoblast differentiation. *J. Bone Miner. Res.* **2005**, *20* (2), 330-40.
63. Fourel, L.; Valat, A.; Faurobert, E.; Guillot, R.; Bourrin-Reynard, I.; Ren, K.; Lafanechère, L.; Planus, E.; Picart, C.; Albiges-Rizo, C., β 3 integrin-mediated spreading induced by matrix-bound BMP-2 controls Smad signaling in a stiffness-independent manner. *J. Cell Biol.* **2016**, *212* (6), 693-706.
64. Suzawa, M.; Tamura, Y.; Fukumoto, S.; Miyazono, K.; Fujita, T.; Kato, S.; Takeuchi, Y., Stimulation of Smad1 Transcriptional Activity by Ras-Extracellular Signal-Regulated Kinase Pathway: A Possible Mechanism for Collagen-Dependent Osteoblastic Differentiation*. *J. Bone Miner. Res.* **2002**, *17* (2), 240-248.

65. Kim, Y.; Renner, J. N.; Liu, J. C., Incorporating the BMP-2 peptide in genetically-engineered biomaterials accelerates osteogenic differentiation. *Biomaterials Science* **2014**, *2* (8), 1110-1119.
66. Bhagoria, P.; Sebastian, E. M.; Jain, S. K.; Purohit, J.; Purohit, R., Nanolithography and its alternate techniques. *Mater. Today: Proc.* **2020**, *26*, 3048-3053.
67. Singh, A.; Shi, A.; Claridge, S. A., Nanometer-scale patterning of hard and soft interfaces: from photolithography to molecular-scale design. *Chem. Commun.* **2022**, *58* (94), 13059-13070.
68. Li, Z. Q.; Guo, P.; Zhou, Y. G., Dip-Pen Nanolithography Enabled Functional Nanomaterials and Their Applications. *Adv. Mater. Technol.* **2021**, *6* (4), 2000897.
69. Yadav, T. C.; Bachhuka, A., Tuning foreign body response with tailor-engineered nanoscale surface modifications: fundamentals to clinical applications. *J. Mater. Chem. B* **2023**, *11*, 7834-7854
70. Cui, J.; Zhang, S.; Huang, M.; Mu, X.; Hei, J.; Yau, V.; He, H., Micro-nano porous structured tantalum-coated dental implants promote osteogenic activity in vitro and enhance osseointegration in vivo. *J. Biomed. Mater. Res., Part A* **2023**, *111*(9):1358-1371.

Supporting Information

Manipulating Stem Cell Fate with Disordered Bioactive Cues on Surfaces: The Role of Bioactive Ligand Selection

Yujie, ZHANG¹ ; Murielle, REMY¹ ; Thierry, LESTE-LASSERRE² ; Marie-Christine, DURRIEU^{1*}

1 Univ. Bordeaux, CNRS, Bordeaux INP, CBMN, UMR 5248, France

2 Univ. Bordeaux, INSERM, PUMA, Neurocentre Magendie, U1215, Bordeaux, France

E-mail : marie-christine.durrieu@inserm.fr

OPN	MSC-N	MSC-D	OB	M1	M2	M3	M4	S0	S1	S2	S2	S4	S5
MSC-N													
MSC-D	N												
OB	N	N											
M1	*	N	N										
M2	*	N	N	N									
M3	*	N	N	N	N								
M4	*	N	N	N	N	N							
S0	*	N	N	N	N	N	N						
S1	*	N	N	N	N	N	N	N					
S2	N	N	N	N	*	N	N	N	N				
S3	*	N	N	N	N	N	N	N	N	N			
S4	*	N	N	N	N	N	N	N	N	N	N		
S5	*	N	*	*	N	*	*	*	*	*	*	*	

Fig. S1 Statistical analysis of OPN after 2 weeks of culture. The statistical analysis was done by one-way analysis of variance (ANOVA) and Tukey's test for multiple comparisons. P values are represented as following * 0.05,). N represented the mean difference was not significant at the 0.05 level. P values are denoted as follows: *p < 0.05. A non-significant mean difference was indicated when p > 0.05.

E11	MSC-N	MSC-D	OB	M1	M2	M3	M4	S0	S1	S2	S2	S4	S5
MSC-N													
MSC-D	N												
OB	N	N											
M1	*	*	*										
M2	*	*	*	N									
M3	N	*	*	N	N								
M4	N	N	*	N	N	N							
S0	*	*	*	N	N	N	N						
S1	*	*	*	N	N	N	N	N					
S2	*	*	*	N	N	*	*	N	N				
S3	*	*	*	N	N	N	N	N	N	N			
S4	*	*	*	N	N	N	N	N	N	N	N		
S5	*	*	*	*	*	*	*	N	*	N	N	*	

Fig. S2 Statistical analysis of E11 after 2 weeks of cell culture. The statistical analysis was done by one-way analysis of variance (ANOVA) and Tukey's test for multiple comparisons. P values are represented as following * 0.05,). N represented the mean difference was not significant at the 0.05 level.

DMP1	MSC-N	MSC-D	OB	M1	M2	M3	M4	S0	S1	S2	S2	S4	S5
MSC-N													
MSC-D	N												
OB	N	N											
M1	*	*	*										
M2	*	N	N	N									
M3	*	N	N	N	N								
M4	*	N	N	N	N	N							
S0	N	N	*	N	N	N	N						
S1	*	*	*	N	N	N	N	N					
S2	*	*	*	*	*	*	*	*	*				
S3	*	*	*	N	N	N	N	N	N	*			
S4	*	*	*	N	*	N	N	*	N	N	N		
S5	*	*	*	*	*	*	*	*	*	*	*	*	

Fig. S3 Statistical analysis of DMP1 after 2 weeks of cell culture. The statistical analysis was done by one-way analysis of variance (ANOVA) and Tukey's test for multiple comparisons. P values are represented as following * 0.05,). N represented the mean difference was not significant at the 0.05 level.

SOST	MSC-N	MSC-D	OB	M1	M2	M3	M4	S0	S1	S2	S2	S4	S5
MSC-N													
MSC-D	N												
OB	N	N											
M1	*	*	*										
M2	N	N	N	N									
M3	N	N	N	*	N								
M4	*	*	N	N	N	N							
S0	*	*	N	N	N	N	N						
S1	*	*	*	N	N	*	N	N					
S2	*	*	N	N	N	*	N	N	N				
S3	*	*	*	N	N	*	N	N	N	N			
S4	*	*	*	N	N	*	N	N	N	N	N		
S5	*	*	*	*	*	*	*	*	*	*	*	*	

Fig. S4 Statistical analysis of SOST after 2 weeks of cell culture. The statistical analysis was done by one-way analysis of variance (ANOVA) and Tukey's test for multiple comparisons. P values are represented as following * 0.05,). N represented the mean difference was not significant at the 0.05 level.

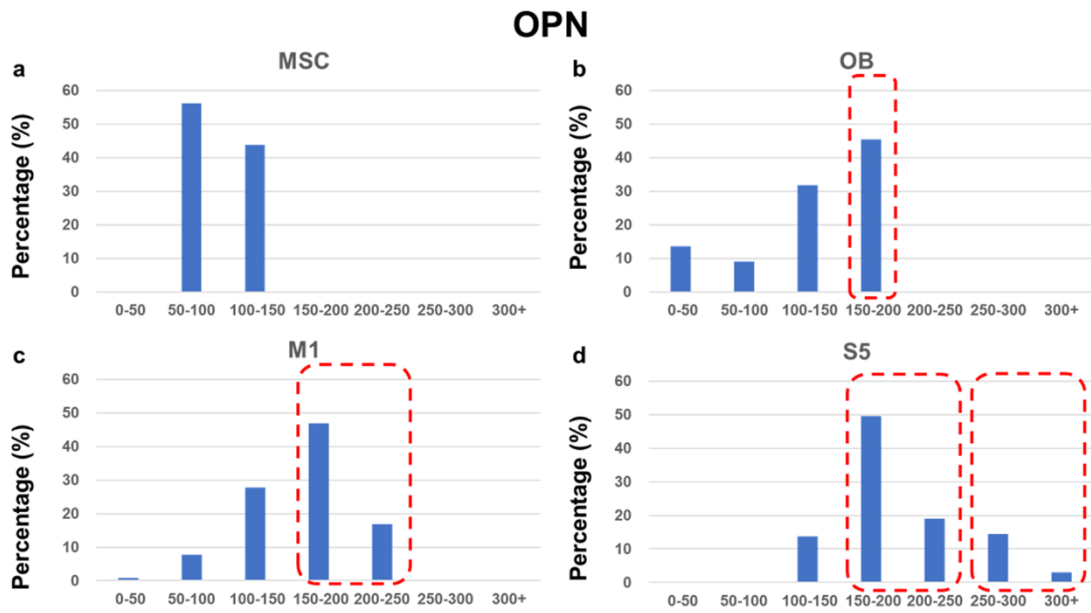


Fig. S5 Class distribution of the immunofluorescence expression of OPN after 2 weeks of cell culture for MSC-N and osteoblasts cultured on glass (controls), and for MSC cultured on M1 and S5. The expressions of OPN higher than that of MSC or osteoblasts on the glass (controls) are highlighted in a dashed red rectangle.

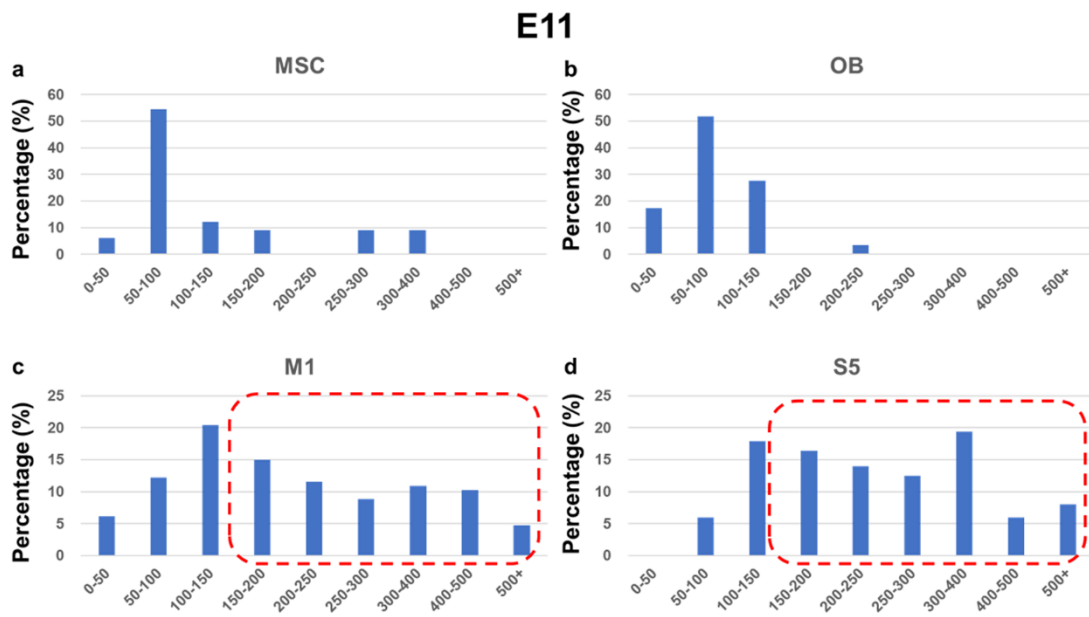


Fig. S6 Class distribution of the immunofluorescence expression of E11 after 2 weeks of cell culture for MSC-N and osteoblasts cultured on glass (controls), and for MSC cultured on M1 and S5. The expressions of E11 higher than that of MSC and osteoblasts on the glass (controls) are highlighted in a dashed red rectangle.

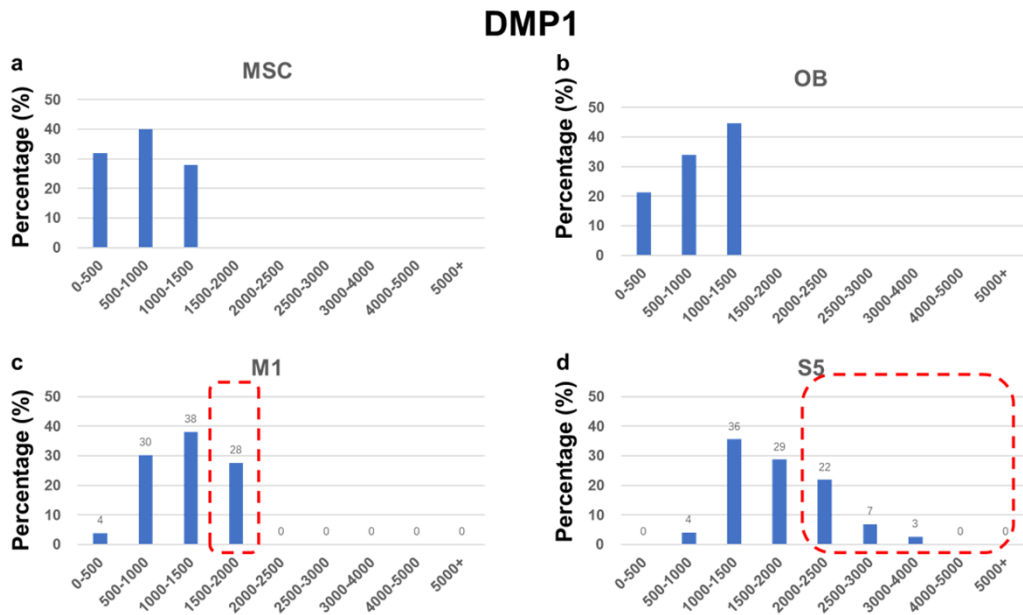


Fig. S7 Class distribution of the immunofluorescence expression of DMP1 after 2 weeks of cell culture for MSC-N and osteoblasts cultured on glass (controls), and for MSC cultured on M1 and S5. The expressions of DMP-1 higher than that of MSC and osteoblasts on the glass (controls) are highlighted in a dashed red rectangle.

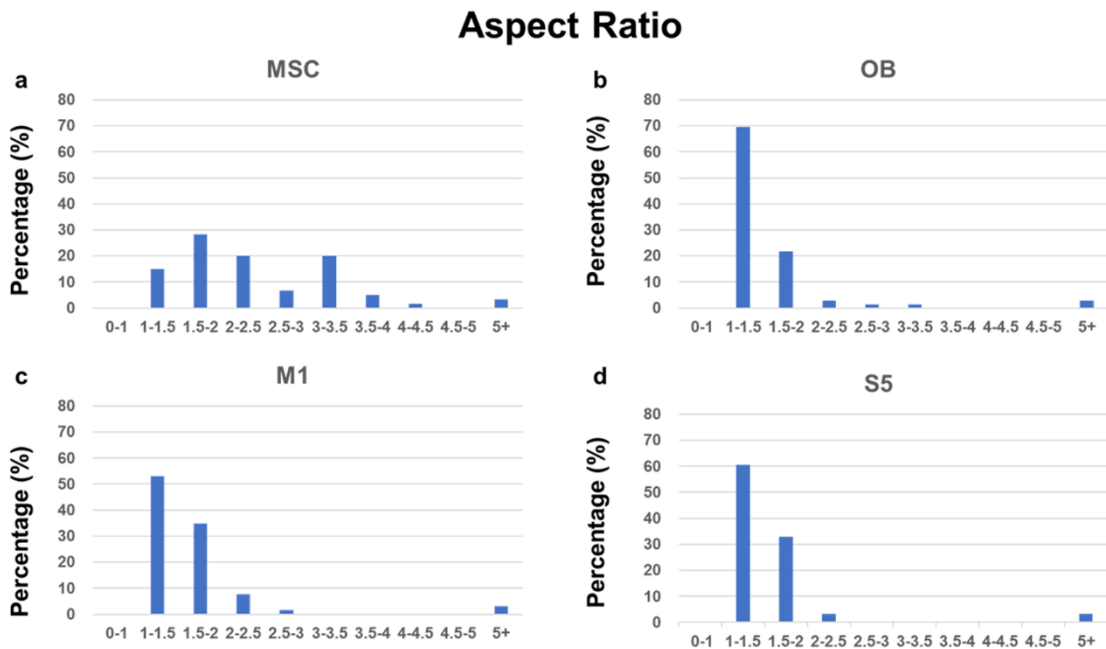


Fig. S8 Class distribution of aspect ratio after 2W a) MSC-N and b) osteoblasts cultured on glass (controls), and for MSC cultured on c) M1 and d) S5.

Circularity

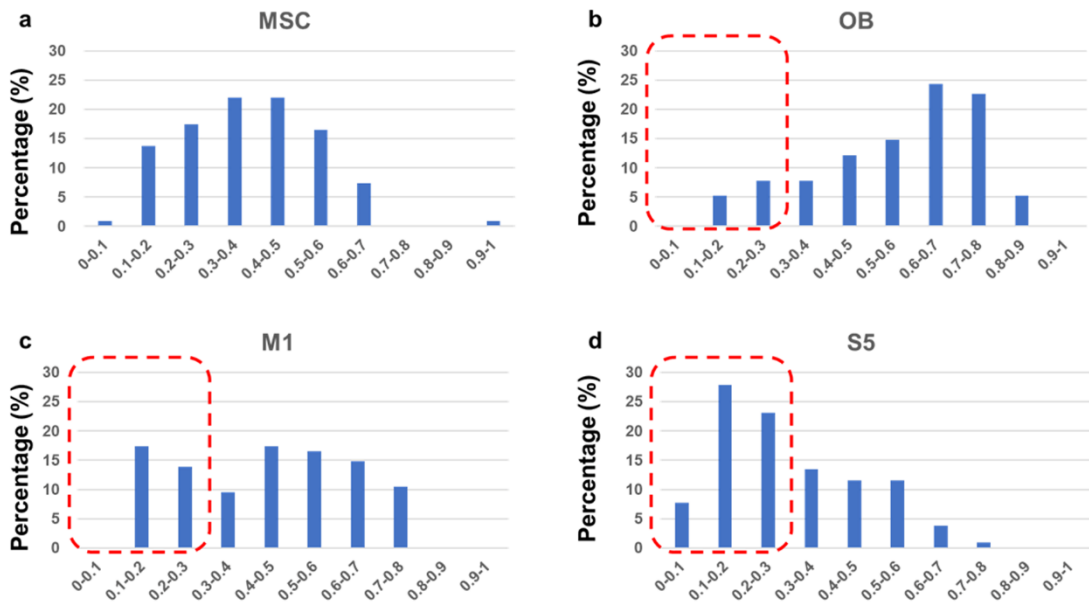


Fig. S9 Class distribution of circularity value after 2W for a) MSC-N and b) osteoblasts cultured on glass (controls), and for MSC cultured on c) M1 and d) S5. The lowest circularity values (ranging from 0 to 0.3) of OB, M1, and S5 were highlighted in red dashed rectangles.

Anisotropy

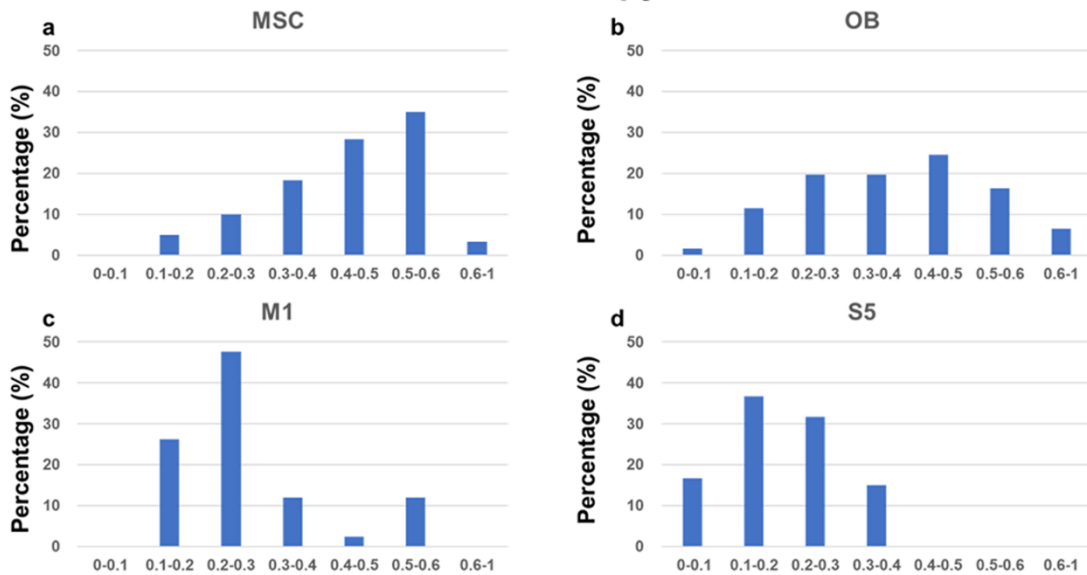


Fig. S10 Class distribution of anisotropy value after 2W for a) MSC-N and b) osteoblasts cultured on glass (controls), and for MSC cultured on c) M1 and d) S5.